JGR Planets

RESEARCH ARTICLE
10.1029/2019JE005953

Key Points:
- The Victoria quadrangle of Mercury encompasses three coeval fault systems
- The three systems were formed by a nonisotropic stress field
- Fault nucleation was controlled by preexisting crustal heterogeneities

Supporting Information:
- Supporting Information S1
- Table S1

Correspondence to:
V. Galluzzi,
valentina.galluzzi@inaf.it

Citation:
Galluzzi, V., Ferranti, L., Massironi, M., Giacomini, L., Guzzetta, L., & Palumbo, P. (2019). Structural analysis of the Victoria quadrangle fault systems on Mercury: Timing, geometries, kinematics, and relationship with the high-Mg region. *Journal of Geophysical Research: Planets*, *124*, 2543–2562. https://doi.org/10.1029/2019JE005953

Received 18 FEB 2019
Accepted 2 AUG 2019
Accepted article online 10 SEP 2019
Published online 16 OCT 2019

Author Contributions:
Conceptualization: V. Galluzzi, L. Ferranti
Data curation: V. Galluzzi
Formal analysis: V. Galluzzi, L. Giacomini, L. Guzzetta, P. Palumbo
Funding acquisition: P. Palumbo
Investigation: V. Galluzzi, L. Ferranti, M. Massironi
Methodology: V. Galluzzi, L. Ferranti, M. Massironi
Project administration: P. Palumbo
Resources: V. Galluzzi, L. Ferranti, M. Massironi, L. Giacomini
Software: V. Galluzzi
Supervision: L. Ferranti, M. Massironi, P. Palumbo
Validation: V. Galluzzi, L. Ferranti, M. Massironi, P. Palumbo
Visualization: V. Galluzzi
Writing - original draft: V. Galluzzi
Writing – review & editing: V. Galluzzi, L. Ferranti, M. Massironi, L. Giacomini, L. Guzzetta

Structural Analysis of the Victoria Quadrangle Fault Systems on Mercury: Timing, Geometries, Kinematics, and Relationship with the High-Mg Region

V. Galluzzi[1], L. Ferranti[2,1], M. Massironi[3], L. Giacomini[1], L. Guzzetta[1], and P. Palumbo[4,1]

[1]Istituto di Astrofisica e Planetologia Spaziali (IAPS), INAF, Rome, Italy, [2]Dipartimento di Scienze della Terra, dell'Ambiente e delle Risorse, Università degli Studi di Napoli "Federico II", Naples, Italy, [3]Dipartimento di Geoscienze, Università degli Studi di Padova, Padua, Italy, [4]Dipartimento di Scienze e Tecnologie, Università degli Studi di Napoli "Parthenope", Naples, Italy

Abstract Three nonparallel fault systems occur in the Victoria quadrangle of Mercury. The most prominent system (Victoria system) includes the NNW-SSE trending Victoria Rupes-Endeavour Rupes-Antoniadi Dorsum (VEA) array, one of the major fault alignments on the planet, and shorter parallel fault arrays. West and northwest of the Victoria system, two additional fault systems with NE-SW (Larrocha system) and NW-SE (Carnegie system) trends, are found. The timing analysis reveals that the three systems are coeval and were active until ~3.7 Ga. Measures of rim offset within faulted craters on the VEA array and on Carnegie Rupes segment of the Carnegie system were used to derive the kinematics of faults and to perform a finite stress inversion, which provides an ENE-WSW trending regional shortening axis. Results of the stress inversion and age relationships, together with geometrical and morpho-structural observations, suggest that the NE-SW and NW-SE systems acted as right-transcurrent and left-transpressional, respectively, at the time when the computed strain field was active. The distribution of the three systems spatially coincides with the boundaries of the high-Mg region and of other regional geochemical terranes. Lateral geomechanical variation of the crust combined with tidal despinning and global contraction processes drove the localization and slip pattern of faults in a kinematically consistent displacement field. Moreover, crustal heterogeneities controlled the lateral changes in density and spacing of fault segments along the VEA. Following the demise of faulting, the established lateral variation of geometry along the VEA favored the growth of volcanic vents at high-permeability segment boundaries.

Plain Language Summary Thanks to the recent completion of the geological map of a wide region of Mercury, named Victoria quadrangle, we observe three main orientations of scarps, which are the surface expressions of fault systems. We find out that the three fault systems formed before 3.7 Ga ago and that the principal force that created these systems had a main WNW-ESE direction. This shortening force should have caused pure compression on the systems perpendicular to its direction and oblique to lateral movements on the rest of the faults, although global tectonic models proposed for Mercury do not expect this deformation scenario in this area. However, we observe that the systems are preferentially located in distinct areas of the quadrangle. They are found within and around a peculiar crustal high-density region with high-magnesium abundance possibly characterized by a high-magma production in the past. We conclude that its activity and density influenced the geometry of faults and their deformation style. Our findings suggest that lateral compositional variations of the crust should be taken into consideration when dealing with global tectonic models of Mercury.

1. Introduction

Mercury's tectonics has been extensively studied at a global scale, revealing that scarps and elongated ridges represent the product of widespread horizontal compressive stresses (e.g., Byrne et al., 2014; Melosh & McKinnon, 1988; Strom et al., 1975; Watters & Nimmo, 2010). In most cases, these landforms have an arcuate morphology and asymmetrical profile and are referred to as *lobate scarps*, which are the surface expressions of thrust faults (Massironi, Byrne, & van der Bogert, 2015; Melosh & McKinnon, 1988; Strom et al., 1975; Watters et al., 2004; Watters & Nimmo, 2010). Symmetrical and narrow ridges named *high-relief ridges* are thought to be the surface expression of buried high-angle reverse faults (Dzurisin, 1978; Massironi

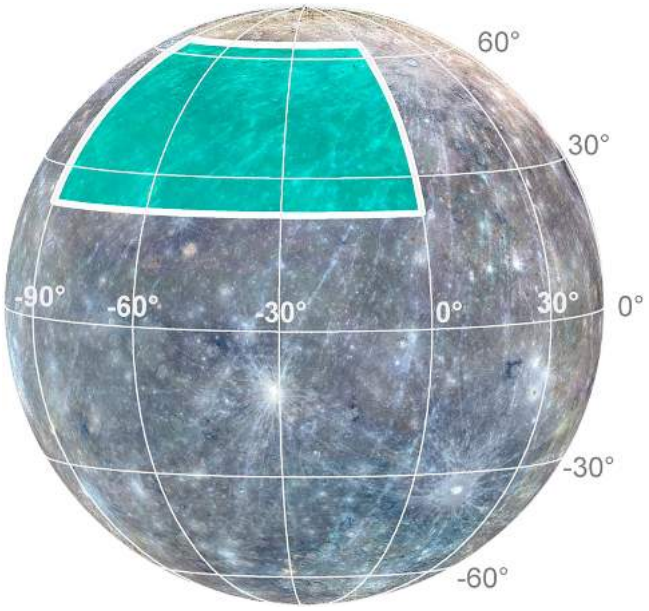

Figure 1. Mercury globe in orthographic projection centered at 25°W and 5° N showing the location of the Victoria quadrangle (cyan area) on the MDIS MD3 basemap v3 with 1,000, 750, and 430 nm as RGB, respectively.

& Byrne, 2015; Melosh & McKinnon, 1988; Watters et al., 2004; Watters & Nimmo, 2010). Lobate scarps and high-relief ridges are mostly found within the cratered plains of Mercury and often merge and align into regional arrays characterized by positive topographic relief on the upthrown fault block. These features have been taken as evidence for the existence on the planet of thick-skinned tectonism (Byrne et al., 2014).

Contraction is also the cause of development of *wrinkle ridges* (Korteniemi et al., 2015; Schultz, 2000; Watters, 1988), which are commonly observed within Hermian most recent volcanic plains and are distinguished from lobate scarps because of the more limited length and lower amount of accrued displacement (Byrne et al., 2014; Watters et al., 2004; Watters & Nimmo, 2010). The development of the wrinkle ridges is related to anticlines above blind thrust faults (Schultz, 2000).

One of the best exposures of lobate scarps and additional shortening landforms is found in the Victoria quadrangle of Mercury (22.5–65°N; 0–90°W, Figure 1). This region encompasses Carnegie Rupes (CR), Victoria Rupes (VR), Endeavour Rupes (ER), and Antoniadi Dorsum (AD). The tectonic scarps that bound the latter three landforms represent one of the most prominent high-terrain bounding fault arrays on Mercury (Byrne et al., 2014), reaching a total length of ~1,500 km in the N-S direction. To the west of this fault alignment, the quadrangle encompasses a large portion of the high-Mg geochemical terrane reported by Weider et al. (2015). In the part of the terrane found in the quadrangle, the concentration of magnesium is the highest detected on the planet (Nittler et al., 2016). Moreover, Namur and Charlier (2017), who investigated the mineralogical variations of Mercury's crust, assess that the high-Mg region (HMR) may register the highest-crustal densities on the planet. On the other hand, the surrounding terrains are likely characterized by lower-crustal densities (Namur & Charlier, 2017).

Thus, the occurrent existence of regionally long fault systems with different strikes and of crustal heterogeneities renders the Victoria quadrangle suitable of providing pivotal insights into the role of density variations in controlling the location and kinematics of fault arrays on Mercury.

In this study, we use MErcury Surface, Space Environment, Geochemistry and Ranging (MESSENGER) mission (Solomon et al., 2007) data and the 1:3 M-scale geologic map of the Victoria quadrangle (H-2; Galluzzi et al., 2016) to analyze the structure and kinematics of the area encompassing CR, VR, ER, and AD and their relationship with the HMR. The detailed fault and timing analysis presented in this paper allowed us to correlate fault geometry and kinematics to Mercury's crustal properties. Comparison of the distribution, geometry, and kinematics of these fault systems with geophysical data and surface chemistry illustrates the mutual relationships between the structural pattern, crustal properties, and composition.

1.1. Global Tectonic Models and Observations

The thrust-related landforms observed on the surface are thought to be related to the planet's global contraction due to global cooling (Strom et al., 1975). Studies report that global contraction started by the end of the Late Heavy Bombardment period (Byrne et al., 2014; Strom et al., 1975), dated back to 4.0–4.1 Ga ago (Bottke et al., 2012; Marchi et al., 2013). Conversely, the current thermophysical evolution models place the start of global contraction well after the Late Heavy Bombardment, at ~1.5 Ga after the formation of the planet (i.e., 3.1 Ga; Tosi et al., 2013).

Indeed, evidence for a geologically recent shortening (Mansurian or younger) has been observed on single thrusts (Banks et al., 2015), or minor fault segments (Watters et al., 2016). Other dating analyses performed on some of the major fault systems show that these vast alignments ended most of their activity 3.5–3.7 Ga ago (i.e., Calorian; Giacomini et al., 2015, 2018). Moreover, analysis on the relationship between craters and faults supports that, while global contraction started before the Calorian (i.e., before ~3.9 Ga), faults began accommodating shortening during the early Calorian (i.e., ~3.9–3.7 Ga), with decreasing strain rates up to recent times (Crane & Klimczak, 2017).

The systematic orientation of structures in some areas of the planet (Melosh & McKinnon, 1988; Watters et al., 2004) strengthened the idea that, besides global contraction, a tidal despinning process influenced Mercury's tectonics in the past (Melosh & Dzurisin, 1978; Pechmann & Melosh, 1979). However, model predictions indicate that tidal despinning alone would have created a globally recognizable pattern of thrusts, strike-slip, and normal faults (Beuthe, 2010; Melosh, 1977), whereas tectonics governed solely by global contraction should have caused isotropic stresses and a random orientation distribution of thrust faults (e.g., Klimczak et al., 2015; Massironi, di Achille, et al., 2015). Since this is not observed at a global scale, it has been suggested that despinning acted concurrently with global contraction during the early evolution of Mercury (e.g., Klimczak et al., 2015; Matsuyama and Nimmo, 2009), with some global contraction reworking inherited despinning faults (Dombard & Hauck, 2008). In this latter scenario, E-W thrusts or joint patterns are predicted if tidal despinning overprints on top of global contraction and where stresses from global contraction are great enough to overcome the frictional resistance to sliding along the faults (Klimczak et al., 2015). Such patterns were observed in the northern smooth plains of Mercury (Crane & Klimczak, 2019).

In addition to global contraction and tidal despinning, it has been proposed that mantle convection must have contributed to shaping Mercury's crust at some time in the planet's history (Grott et al., 2011; King, 2008; Michel et al., 2013; Redmond & King, 2007; Tosi et al., 2013). For some authors, mantle convection could be active at present (Grott et al., 2011; King, 2008; Redmond & King, 2007). Recent thermal models do not exclude this scenario, albeit it is more likely that the mantle is currently in a conductive state (Michel et al., 2013; Tosi et al., 2013). The occurrence of fold-and-thrust systems where extensive thrusts are bounded by lateral ramps that indicate a constant vergence has been suggested to be one surface evidence for the contribution of mantle convection to the total shortening (Massironi, di Achille, et al., 2015).

2. Data and Methods

2.1. Base Data

We use the MESSENGER Mercury Dual Imaging System instrument wide-angle camera and narrow-angle camera images (Hawkins et al., 2007), either as single frames, partial mosaics, or global mosaics. The latter are (1) the map-projected Basemap Data Record, (2) the map-projected High-Incidence angle basemap illuminated from the West, and (3) the map-projected High-Incidence angle basemap illuminated from the East, described in Denevi et al. (2018). We processed single frames and partial mosaics using the Integrated Software for Imagers and Spectrometers v3 of the United States Geological Survey, starting from raw Experiment Data Record frames. These were projected onto a reference sphere of 2,439.4-km mean radius (as of MESSENGER end-of-mission data sets) and controlled by the latest available United States Geological Survey Mercury shape model (Becker et al., 2016).

The studied faults were taken from the 1:3 M-scale geologic map of the H-2 quadrangle (Galluzzi et al., 2016) and updated using the above-mentioned end-of-mission basemaps, high-resolution mosaics, and the 665 m/pixel digital elevation model (DEM) of Becker et al. (2016). Fault-related landforms were mapped following a "structural approach" as described in Galluzzi (2019), and different symbology was used to distinguish (a) "thrusts, certain," where there is a clear scarp associated to a clear topographic offset visible both in the basemap and the digital terrain model (DTM), whose intersection with the footwall ranges from moderately to very sharp morphology, likely corresponding to a surface-breaking thrust fault; (b) "thrusts, uncertain," where there is no sharp intersection with the footwall, likely corresponding to a near-surface thrust fault; (c) "other faults, certain," where there is a crisp lineament (not associable to exogenic factors, e.g., impact-cratering lineations) visible at least in one of the basemaps and associated to a slight topographic offset in the DTM, but with no clear sense of vergence; (d) "other faults, uncertain," where the lineaments are less clear in the basemap and mostly inferred from the DTM; and (e) "wrinkle ridges," where there are small ridges with associated scarps that often show changes in vergence, visible both in the basemap and in the DTM if not too small, and located principally on the youngest volcanic plains. Although wrinkle ridges are often associated to thrusts (with shorter length compared to the other mapped thrusts), we kept their morphological term to make them stand out on the regional structural framework.

2.2. Structural and Kinematic Analysis

The structural study of the area was done by means of spatial and morphological analysis, rendered in rose diagrams. The rose diagrams were built using the Polar Plots tool for ArcGIS by Jenness (2014) that can

automatically plot the geodesic azimuth of the mapped faults into a rose of length-weighted trend bins, such that emphasis is given to the longest faults. We did not divide each fault into further geometrical parts to calculate inner strike variations but calculated their average geodesic azimuth from tip to tip by using Tools for Graphics and Shapes by Jenness (2011). We selected to plot the data into 5° trend bins to account for a rose of 72 directions, which is enough for detecting preferential trends at the regional scale.

The kinematic analysis was performed using the method described in Galluzzi et al. (2015) that uses faulted craters as markers to quantify fault-slip parameters (Figure 2). The basis of this method is similar to the split crater analysis of Pappalardo and Collins (2005) that aims at finding the extensional strain registered by craters on Ganymede, even when these are crosscut by several faults. Our method aims at locally characterizing a single thrust fault plane that crosscuts a crater. It is based on the assumption that (a) the crater pristine shape was circular before faulting; (b) the preexisting local topography was "uniform," such that the current offset between the hanging wall and the footwall part of the crater reflects the actual fault vertical component of the net slip. The first assumption is true for most craters, since regardless of the magnitude of the gravitational field, the most probable impact angle for all planetary bodies is 45° (Gilbert, 1893; Shoemaker, 1962), but only impact angles below 10–15° can generate a noncircular shape (Gault & Wedekind, 1978; Bottke et al., 2000; see also Kenkmann et al., 2014). The second assumption needs to be verified locally for each faulted crater. However, it is conceivable that the existing regional-scale slopes (e.g., the long-wavelength topography, Zuber et al., 2012) do not significantly affect the vertical offset of faulted craters, whose diameter is usually much smaller (Galluzzi et al., 2015).

As a first step, a 2D analysis of the split crater morphology is done on monochrome images in map view to estimate the horizontal slip (Figure 2a). First, a circle is drawn either on the hanging wall or on the footwall rim of the crater (Figure 2b). We use the CraterTools software (Kneissl et al., 2011) to build a map-projection-independent circle; however, this procedure is always carried out using a stereographic projection centered on the crater to minimize visual shape distortions. Second, we fit a new copy of the first circle on the part of the rim not mapped in the first step (Figure 2b). Then, the horizontal displacement between the two circle centers (Δx) and the trend of the joining segment (i.e., the slip trend) are measured (Figure 2b). If the crater is large enough, these steps are repeated at least twice and by different mappers in order to increase the mapping confidence and estimate the uncertainty on both Δx and the slip trend. We stress that the Δx may correspond to the fault's "heave" (i.e., horizontal offset perpendicular to the fault strike) only if a pure dip slip (i.e., slip trend perpendicular to the fault strike) is recorded.

In a second step, a 3D analysis of the displaced crater is done by using the 665 m/pixel DEM (Becker et al., 2016; e.g., Figure 2c) to estimate the vertical offset. In Galluzzi et al. (2015), topographic profiles are built along the slip direction to estimate the vertical offset between the footwall and the hanging wall of the fault. However, a topographic profile provides single point information on the maximum and minimum heights, and the available DEM does not provide enough accuracy for the measurements. Here we made a spatial slope analysis of the DEM in the crater area to select coupled polygons at the footwall and the hanging wall of the fault (either rim-rim or floor-floor couples), each characterized by homogeneous shallow slope and comparable elevation (cf. Figures 2c and 2d). The cloud of DEM elevation measures in the sampling areas was used to estimate a reliable elevation uncertainty for each polygon. Finally, we calculated the vertical offset ("throw," Δh) across the thrust by subtracting footwall and hanging wall elevation. The obtained values of the slip trend, Δx and Δh, along with the fault strike measured where the fault crosscuts the crater, allowed to estimate the complete fault geometry by applying the following formulas (Galluzzi et al., 2015):

$$\varsigma = \tan^{-1}(\Delta h/\Delta x) \tag{1}$$

$$\delta = \tan^{-1}(\tan\varsigma/\sin\varphi) \tag{2}$$

$$\lambda = \cos^{-1}\left(f_1 s_1 + f_2 s_2 + f_3 s_3\right), \tag{3}$$

where ς is the slip plunge, δ is the true dip of the fault, φ is the angle between the slip trend and the fault strike, and λ is the fault's rake; f_{1-3} and s_{1-3} are the direction cosines of the fault strike and slip trend unit vectors, respectively (where the fault strike is considered as a line with 0° plunge; see also Galluzzi et al., 2015). Because faulted craters were found along faults with different strikes, the method illustrated above provides estimations of the natural variability of fault kinematics. The faulted crater data were used to assess the finite

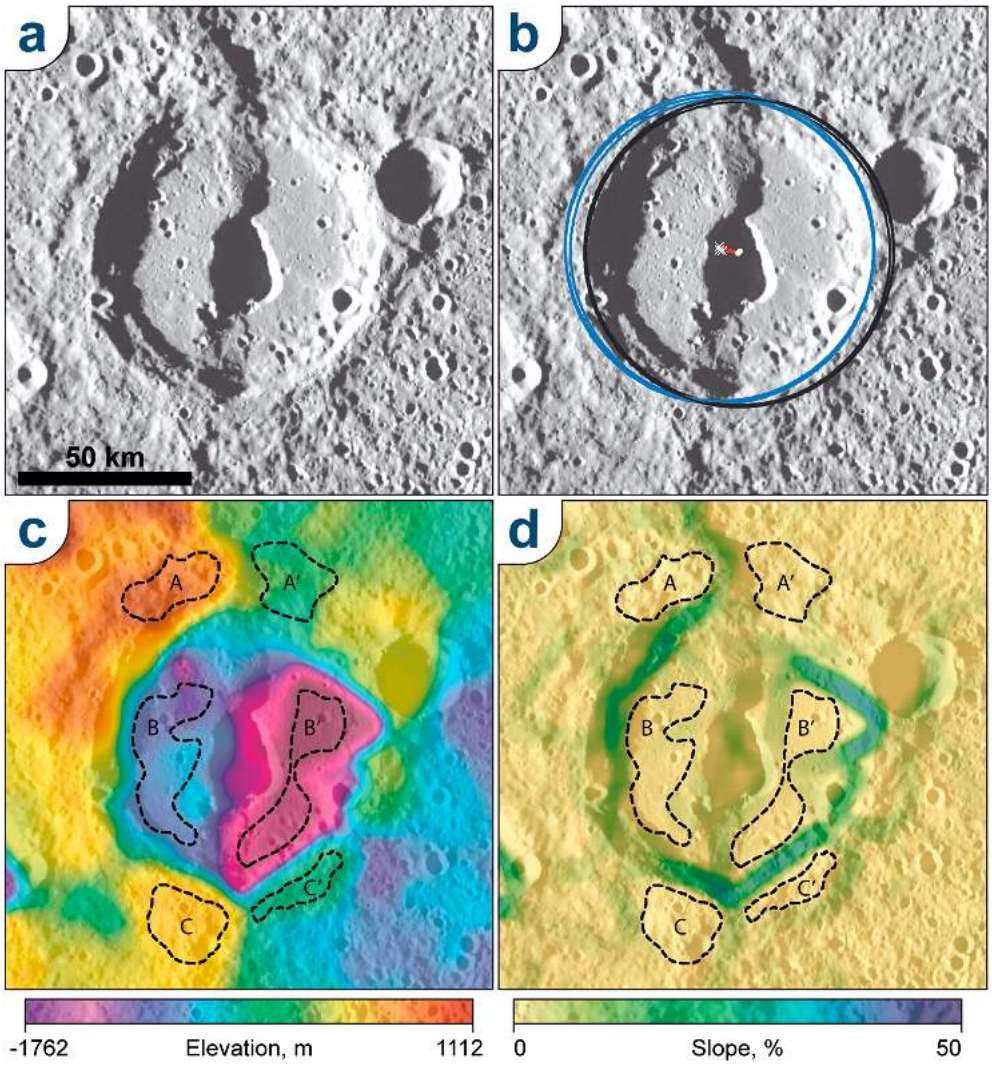

Figure 2. Geddes crater reported as an example for measuring horizontal and vertical offsets of faulted craters: (a) MDIS HIW basemap v2 showing the clean image in stereographic projection centered at the crater centroid (27.1°N; 29.6°W); (b) circles fitting the hanging wall part of the crater (black) versus their copies fitting the footwall part of the crater (blue). Circle centers are also shown for the hanging wall (white dot) and the footwall (white cross). The horizontal offset in the slip direction is measured along the red lines (from cross to dot); (c) USGS DEM v2 (Becker et al., 2016) on top of the basemap in (a). The dashed black outlines show the areas where the elevation was measured to calculate the vertical offset; (d) slope map processed from the DEM in (c) as rise percentage (where 100% = 45° slope) on top of the basemap in (a). The dashed black outlines indicate areas of relatively shallow slopes and comparable heights. The areas are marked with a letter that couples the polygons at the hanging wall (e.g., A) with those at the footwall (e.g., A′).

strain field by applying a stress-inversion analysis that requires a variability in fault strike and slip data (e.g., Angelier, 1979). The stress-inversion analysis is made by means of the PBT-axes (or pressure-tension) method (Sperner et al., 1993) and processed using the Tensor software by Delvaux and Sperner (2003).

2.3. Timing Analysis

The fault timing analysis was done by following the technique described in Tanaka (1982), which relies on the principle that the density of impact craters superposing a linear feature depends on the area defined by the crater diameters. This method was described as the buffered crater counting (BCC) technique by Fassett and Head (2008) and it has hitherto been used principally for dating valley networks (Bouley et al., 2010; Fassett & Head, 2008; Hoke & Hynek, 2009) or fault systems (Fegan et al., 2017; Giacomini et al., 2015, 2018; Kneissl et al., 2015; Yue et al., 2017). Each linear feature encompassed in the fault system will have as many buffers as the counted craters, and the size of the buffers (Sbuffer) depends on the formula:

$$\mathrm{Sbuffer} = \mathrm{E}\times\mathrm{R} + 0.5\times\mathrm{W}f, \quad (4)$$

where E is an empiric ratio of the ejecta extent from the counted crater center with respect to the counted crater radius R, and W*f* is the mapped linear feature width. The BCC analysis was done by using the CraterTools (Kneissl et al., 2011) and the Craterstats2 software (Michael & Neukum, 2010). In our calculations, we choose a W*f* of 4 km to encompass the uncertainty of the line drawing, and we considered an ejecta extent of 2R with respect to the crater center.

3. Results

3.1. Structural Framework of the H-2 Quadrangle

Figure 3 shows more than 400 structures with a shortening component of motion updated from the geologic map by Galluzzi et al. (2016). We also show the main terrain units, which include, from the oldest to the youngest, intercrater plains, intermediate plains (ImP), and the northern volcanic plains (NVP; Galluzzi et al., 2016). Faults are distinguished based on their morphology and kinematic nature. The structural scheme of the H-2 quadrangle shows a sharp difference in the trend of structures between an eastern and a western sector (Figure 3). In general, we observe that the eastern sector is dominated by the Victoria Rupes-Endeavour Rupes-Antoniadi Dorsum (VEA) thrust alignment. In contrast, the western sector shows dominant NE-SW and subordinate NW-SE trending structures, which are mostly faults of more limited length than the lobate scarps of the eastern sector. This structural dichotomy is enhanced by a less-populated zone of fault-related landforms (~400 km wide) observable around 45°W. This zone corresponds to a topographic bulge (hereafter the VEA bulge, see Figure 4; fault-bounded high terrain in Byrne et al., 2014).

Based on the inspection of Figure 3, three main fault trends are distinguished (see rose diagrams in Figure 4): a ~NNW-SSE system, a ~NE-SW system, and a less-populated ~NW-SE system. The first one has strikes ranging from 0° to 20° and from 155° to 180° and is predominant in this area, thus we refer to it as the "Victoria system" (VS, blue faults in Figure 4). The second one ranges mainly from 20° to 80° and encompasses short fault segments with no association to prominent topographic features. We use the Larrocha crater located in the middle of the area crosscut by these faults to designate this system as "Larrocha system" (LS, green faults in Figure 4). The third system comprises fewer faults than the previous ones and ranges between 100° and 155°; it encompasses the CR thrust, thus we refer to it as the "Carnegie system" (CS, purple faults in Figure 4). Wrinkle ridges, here mapped as an independent morpho-structural category, are mostly confined to the NVP and more randomly oriented, although they show preferential ~ENE-WSW and NNW-SSE strikes (pink rose diagram, Figure 4).

3.2. Geometric Analysis of Fault Systems

In order to better elucidate the characteristics of the three main fault systems observed within H-2 (Figure 4), we defined a hierarchical subdivision into (1) systems (as described in the previous paragraph); (2) arrays; (3) sectors; and (4) segments. In this scheme, segments represent a single mappable end-member (i.e., a single fault-related landform), and systems are defined by the main azimuthal sets found through rose diagram analysis. Arrays are identified by analyzing the along-trend continuity of fault segments pertaining to a system. Sectors are identified by analyzing the segments spatial distribution and clustering within long arrays, so they represent a further subdivision of the arrays. Because LS and CS are more scattered than VS, their arrays are often composed by just one sector.

3.2.1. The VS

This system encompasses structures associated with an alternation of high- and low-standing terrains that constitute a ~1,600-km wide zone (from 5°W to 50°W, Figure 4). Four distinct NNW-SSE arrays pertaining to the VS are recognizable (Figure 4, VS). The VEA array is the largest alignment in the system in terms of development and morphological relief. Given the importance of this array, a higher-resolution mapping was done using Mercury Dual Imaging System narrow-angle camera frames (Supporting Information, Figure S1) and is presented in Figure 5. The existence of the prominent VR, ER, and AD, and the laterally varying development of faults, allows three sectors to be distinguished. Moreover, the array is characterized by the presence of three volcanic vents (Galluzzi et al., 2016; Thomas et al., 2014a) that broadly coincide with systematic changes in fault zone segmentation and help defining the limits between the sectors. The VR sector (VEA/*VR*) is characterized by more than 550 km long and almost continuous west-dipping thrust (cf.

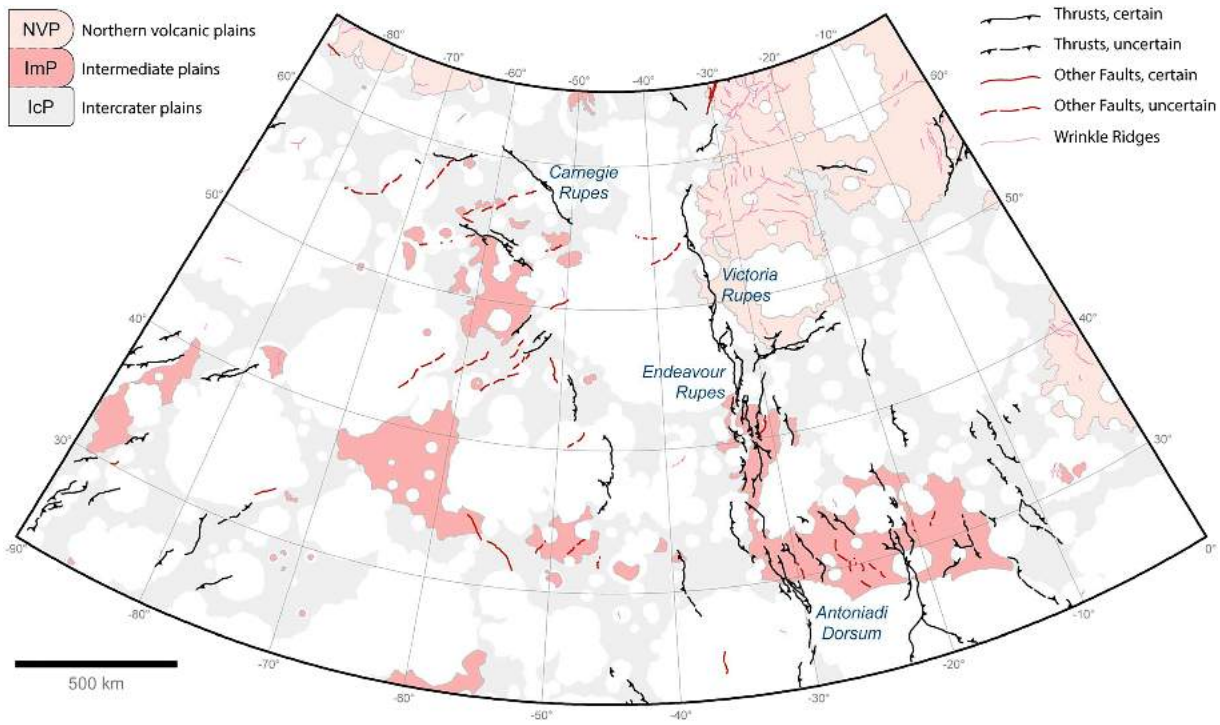

Figure 3. Simplified version of the geological map in Galluzzi et al. (2016), where only the main geological units are displayed in the background and faults on the foreground in Lambert conformal conic projection centered 45°W and standard parallels at 30°N and 58°N (the scale is true at this latitudes).

Figure 4, VS and Figure 5). The rectilinear trace of the thrust swings eastward to the north and its northern tip is less than 30 km away from the vent-bearing Namatjira crater (Figure 5). Conversely, the ER sector (VEA/*ER*) is characterized by several segments scattered within a ~150-km wide fault zone. It encompasses mainly west-dipping thrusts and cuts across an elongated ImP area (cf. Figure 3). In this sector, the complexity of the array arises from the segments length, geometry, and distribution. Indeed, frequent changes in trend and dip are observed, with the development of backthrusts and pop-up features. The transition between the poorly segmented VEA/*VR* sector and the highly segmented VEA/*ER* sector occurs close to the vent-bearing Enheduanna crater (Figure 5). The sector narrows to the south forming a bulk lozenge-shaped fault zone, which is partly covered by the younger Holbein impact (Figure 5). Finally, the AD sector (VEA/*AD*) actually starts at the vent-bearing Geddes crater, which marks an abrupt narrowing and change in fault trend of the fault zone, and heralds the end of the VEA array in this quadrangle.

Array VS-1 is composed of few west-dipping segments with a weak density of faults as highlighted by the kernel density in Figure 4. Two unconnected sectors are recognized. The northern one, *1a*, faces ER that is located 400 km to the east, while the southern one, *1b*, faces AD 255 km to the east. The vergence and trend of both *1a* and *1b* is coherent with the position of ER and AD, but they do not mark significant changes in relief. On the contrary, they stand on top of the VEA bulge. Array VS-2 is located to the east of VEA/*AD* and is scattered across a ~220-km wide zone that develops mostly along the boundary of a topographic high. The major segments within the array are mostly east dipping, thus opposite to the VEA/*AD* main segments. Similarly, Array VS-3 comprises widely spaced fault segments that also dip to the east, but they are relatively less developed and more scattered. In the southern part of the quadrangle, the VEA, VS-2, and VS-3 arrays are on average spaced by ~380 km (see Figure 4, VS).

3.2.2. The LS

The LS is developed in the western part of the quadrangle, almost totally west of the VS. Although less prominent than the VS, the LS is scattered across a wider zone. The majority of the fault segments were mapped as "other faults," because their scarp is not clearly visible. Within the system, we distinguished three main arrays (Figure 4, LS). LS-1 and LS-2, to the north, are characterized by relatively long segments that were mapped based on slight shadows and topographic evidence. The longest array, LS-3, is constituted by

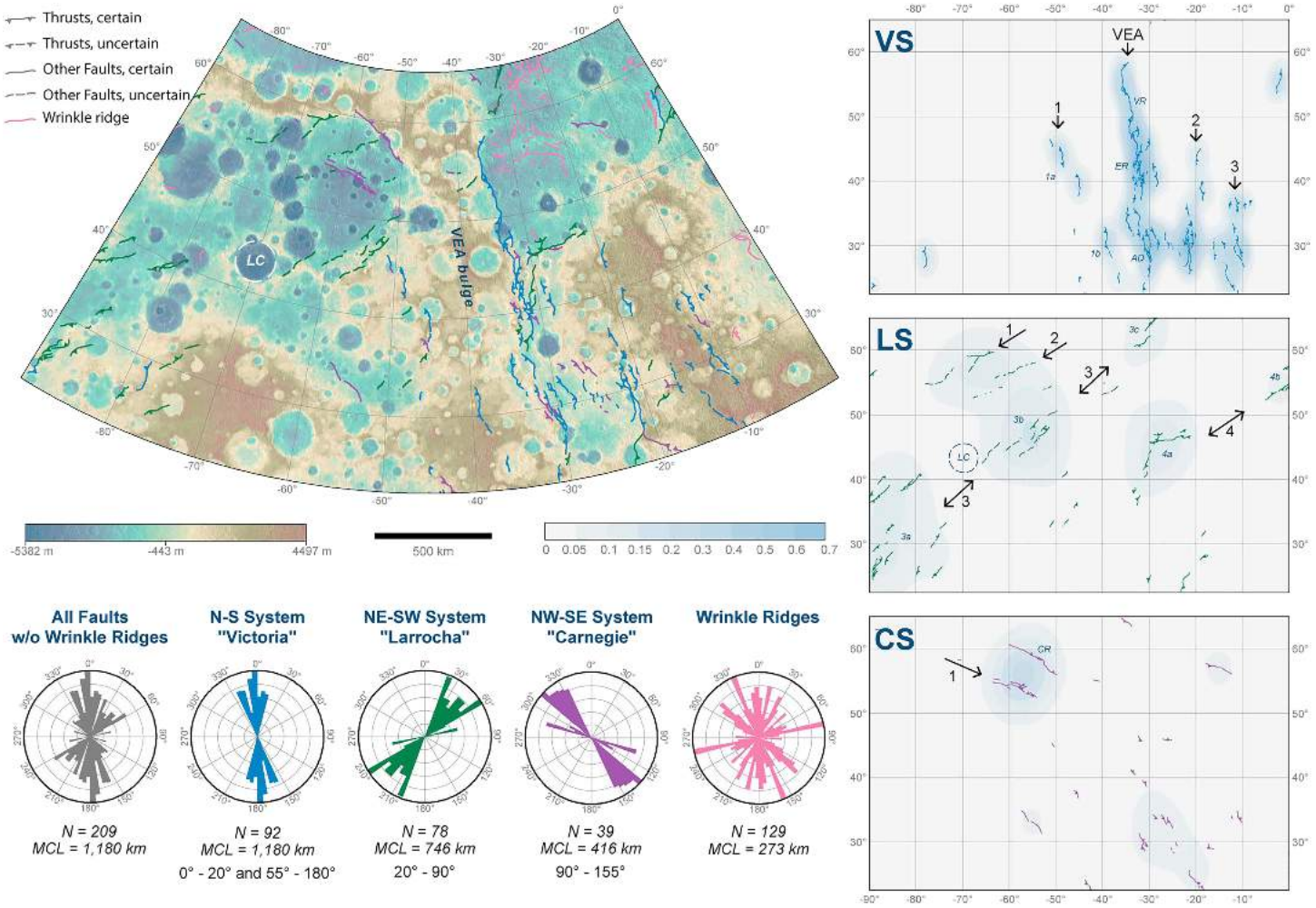

Figure 4. Rose-plot analysis of the structural scheme of H-2 quadrangle. The first four rose plots show the trend analysis weighted by fault length, divided into 5° trend bins, of all faults (gray plot), N-S faults ("Victoria" system, blue), NE-SW faults ("Larrocha" system, green), and NW-SE faults ("Carnegie" system, purple). Wrinkle ridges are excluded from those plots and are shown separately in the fifth plot. N represents the number of included faults, MCL is the maximum cumulative length of the largest bin; the colored ranges indicate the azimuth range considered for each plot (in a 180° domain). Top left: USGS topography on top of HIW mosaic, overlapped by all faults with the colors corresponding to the pertaining system (legend just shows the symbols); Lambert conformal conic projection centered at 45°W longitude with standard parallels at 30°N and 58°. Right: H-2 quadrangle showing VS, LS, and CS alone, overlapped by arrows and numbers indicating the main fault arrays (larger black numbers) and sectors (smaller italic numbers) within each system in equirectangular projection centered at 43.75°N, 45°W. Letters indicate Victoria Rupes (VR), Endeavour Rupes (ER), Antoniadi Dorsum (AD), Victoria-Endeavour-Antoniadi array (VEA), Carnegie Rupes (CR), and Larrocha crater (LC), whose locations are indicated by a dashed circle. The shaded background indicates kernel density of faults from low (light gray) to high (gray-blue).

three noncontiguous sectors. Sector *3a* comprises short scattered segments; Sector *3b* encompasses longer segments, less prominent in terms of topography; and Sector *3c* apparently runs at the northern terminus of VEA/*VR*. It is worth noting that most of the faults, and particularly those forming *3a* and *3b*, are located parallel to the boundary between a low-elevation and a high-elevation terrain. Further, Sectors *3a* and *3b* are separated by a low-standing terrain with no evidence of faults and occupied by the Larrocha crater. Sectors *3b* and *3c* are separated by the VEA bulge. Indeed, faults associated to Sector *3c* run across the eastern part of the bulge and terminate in the northern part of the VEA/*VR* sector. To the east of the VEA bulge, a fourth array, LS-4, is located at the contact between NVP and ImP (cf. Figure 3). The array is divided into two separate sectors more than 500 km from each other. Sector *4a* terminates to the west at the limit between VEA/*VR* and VEA/*ER*, where Geddes volcanic vent occurs, and is composed of north-dipping faults. Whereas Sector *4b*, at the limit with the Hokusai quadrangle to the east, is composed of segments with southerly dip.

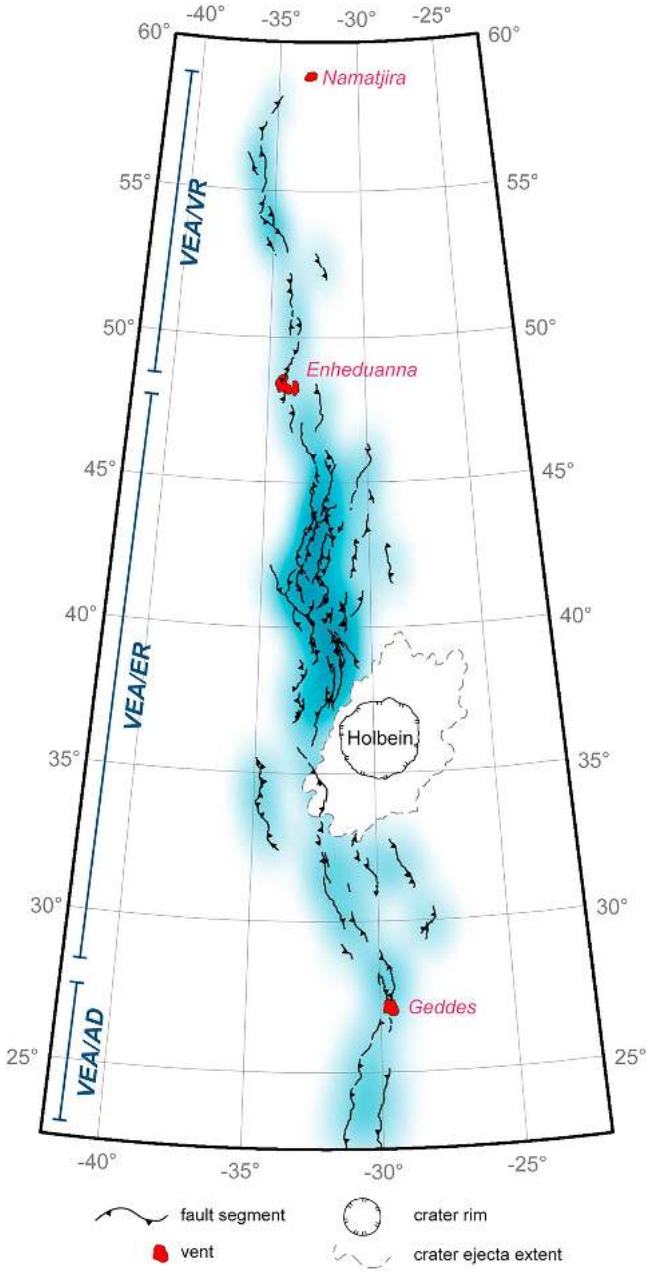

Figure 5. Detailed mapping of the Victoria-Antoniadi-Endeavour fault array in Lambert conformal conic projection centered at 32°W and with standard parallels at 30°N and 58°N. The array sectors VEA/*VR*, VEA/*ER*, and VEA/*AD* are also indicated from north to south, respectively. Holbein crater is taken as a reference impact since it is supposed to cover part of the VEA/*ER* sector. The location of three known volcanic vents (Kerber et al., 2009) is also indicated. For scale, the crater diameter is 110 km.

3.2.3. The CS

The CS is composed of a few scattered fault segments (Figure 4, CS). In particular, the southern CS segments are very short (tens of kilometers) and merge with VS segments. The most developed faults of this system are found in the northern part of the quadrangle. In particular, CR fault to the north is a 330 km long, NE-dipping thrust. To the south of CR, Array CS-1 includes discontinuous parallel segments, with a total length similar to CR. These segments are interfingered with LS-2 segments, creating a lozenge-shaped pattern at 30° angles in map view (Figure 4, CS and LS). Both arrays include mainly northeast-dipping thrusts, antithetic to the west-dipping thrusts of VEA/*VR* to the east. The CS-1 array bounds to the northeast, a low-elevation area, which is the lowest plain in the quadrangle (excluding impact-related floors). CR bounds the western border of the northern part of the VEA bulge. Further west and around 60°N latitude, the VEA bulge turns progressively toward west with an E-W orientation.

3.3. Relative Ages of Fault Systems

The VS and the LS include most of the H-2 faults and thus a higher number of countable craters than the CS. Thus, the BCC analysis was performed only on selected arrays pertaining to the VS and LS. In particular, we analyzed the western faults of the LS and the VEA array of faults. The results for both systems are shown in Figure 6, where a clear overlapping of both cumulative crater frequency distributions is visible. Thus, the VEA array and LS are coeval. Moreover, considering the interfingered relationship between the CS and LS, and the CR as a backthrust associated to the formation of the northern VEA bulge, it is reasonable to consider the CS coeval with the other faults in the area. For completeness, we fitted the resulting crater frequency distributions with the production function developed for porous material on Mercury by Le Feuvre and Wieczorek (2011), following the assumption that the first few kilometers of crust are highly fractured and weaker (Schultz, 1993). The ages are obtained by fitting craters larger than 3 km. Both age-fits are within the same error range, thus the two systems are coeval and, for the considered production function fit, date back to ~3.7 Ga.

3.4. Kinematics of Crater-Cutting Faults and Stress Inversion

Six craters crosscut by faults of the VEA array and the CS were analyzed (Figure 7), and the average fault-slip data results are listed in Table 1 (the measurement data for each crater are presented as Table S1). The map-view analysis of Geddes crater is shown in Figure 2, while the other faulted craters are reported as Figures S2 to S4.

The dip angles estimated from the crater offset are lower than those presented in Galluzzi et al. (2015). Here we use a newer and more complete DEM (Becker et al., 2016), and the use of sampling areas for estimating the elevation in the hanging wall and footwall blocks as described above resulted in a lower-statistical error on the vertical offset. On average, we find that the VEA fault dip angles are very shallow (6°–10°, Table 1), and the CR fault plane is steeper (28° to 52°, Table 1). Regarding data acquired on small craters, uncertainty rises from resolution limits. In the case of CR/Duccio-β and CR/Duccio-γ, the craters might have formed when the fault had already developed a prominent scarp and the small impacts could not reset the preexisting topography, thus inheriting a vertical offset before being faulted themselves. This case certainly leads to an overestimation of δ. In the case of ER/unnamed, a morphological inspection reveals that the crater might have formed before the fault, but because the fault scarp is not prominent, the stereo DEM resolution is not enough to reveal its real vertical

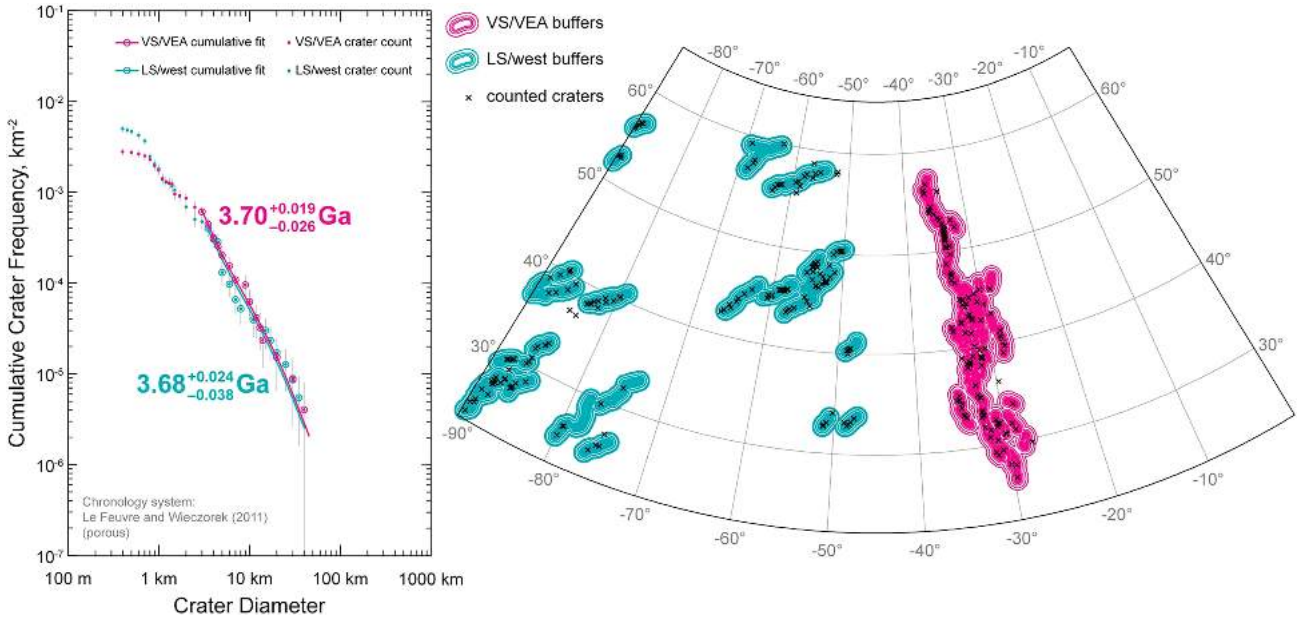

Figure 6. Buffered crater counting results. Left: comparison between the CSFD extrapolated from the VEA array and the western faults of the LS. Right: location of the VEA and western LS buffers. Counted craters (a total of 94 for VEA and 128 for western LS) are signed just by a black cross for output-scale reasons since many are smaller than a few kilometers.

offset. This observation can lead to an underestimation of δ. Further underestimation of δ can depend on the presence of the secondary backthrust associated to AD that crosscuts Geddes crater. In fact, although AD/Geddes has a quite sharp rim that permits a precise fit of the circles with low-statistical error, the presence of a secondary backthrust could enhance the shortening registered by the crater.

In this view, it is possible that fault dip angles along the VEA are steeper than measured. A possible underestimation of fault dip angles cannot be predicted by the statistical error analysis. However, if we decrease the value of Δx of AD/Geddes by 50% to empirically remove the effect of a secondary thrust, or if we increase the value of Δh of ER/unnamed by 200% to account for a severe lack of DTM resolution that would smoothen the topography, we still get δ values lower than 20°. The presence of low-angle thrusts (at least lower than 20°) observed along this array will be discussed further on in the paper.

The estimated fault rakes are mostly dip slip (i.e., ~90°), except for the rake derived from CR/Duccio-α (61 ± 31°). The large uncertainty is due to its irregular and degraded rim that can be fitted by different set of circles (see also Figure S4). Using the fault-slip data derived from faulted crater analysis (Table 1), we performed a stress inversion to derive the stress field associated with crater deformation (Figure 8). We included data from both the VEA and the CR, because they are kinematically coeval and refer to the same regional stress field.

4. Discussion

4.1. Displacement Field and Age of Faulting

The inversion of kinematic data derived from faulted craters (Figure 8) shows that the maximum horizontal compressional stress $\sigma 1$ that accompanied displacement on the VEA (and reasonably of the entire VS) and CS thrusts has an ENE-WSW trend. Unfortunately, no crater crosscut by the LS faults provides quantitative fault-slip data, and thus, we could not characterize the kinematics of the latter fault system. Results of stress inversion, age constraints on faulting, and the geometry of the LS faults offer a chance to circumvent this problem and characterize the complete displacement field in the quadrangle. BCC results give an age of ~3.7 Ga for VS and LS, and the stratigraphic relationships show that a segment of the VEA/*VR* sector cuts the NVP (Figure 3). This area of NVP is likely older than the age estimated for the effusive volcanism events (i.e., 3.5 Ga, Byrne et al., 2016), because of its darker color and higher number of superimposed impacts with respect to the smooth plains located at the north pole (Figure S5). Stratigraphy and BCC are thus in accordance, and

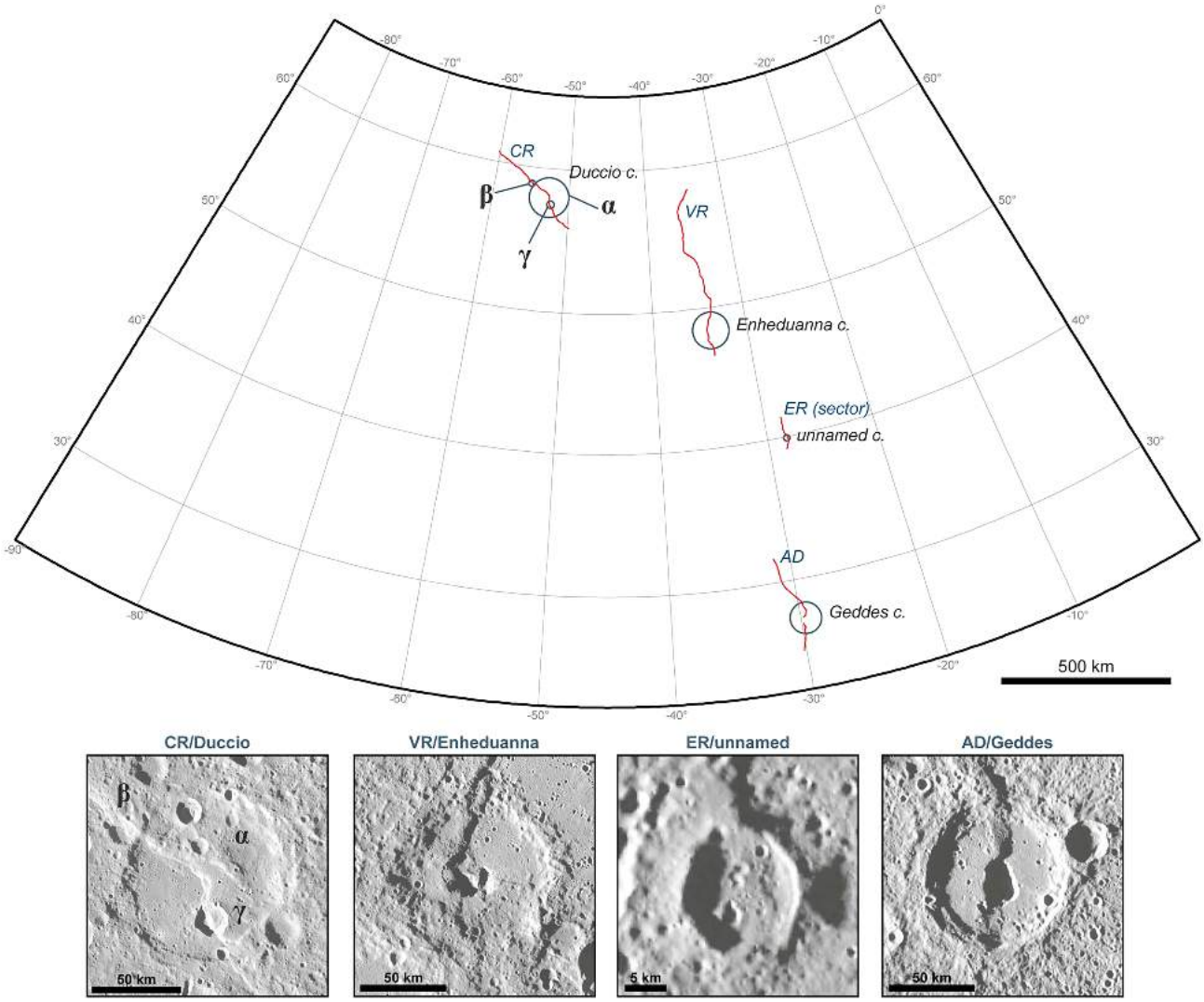

Figure 7. Location of the analyzed faulted craters: CR = Carnegie Rupes cutting Duccio crater (Duccio-α) and two other unnamed small craters (Duccio-β and Duccio-γ); VR = Victoria Rupes cutting Enheduanna crater; ER = a segment of Endeavour Rupes sector cutting an unnamed small crater; AD = Antoniadi Dorsum cutting Geddes crater.

hence, the inversion of kinematic data extrapolated from CR and the VEA array refers to an early Calorian stress field until ~3.7 Ga. This stress field involves also the nearby and coeval LS, which is partly interfingered with CS as described before.

The orientation of $\sigma 1$ forms a low angle with respect to the trend of LS faults (Figure 4, green faults). Under this scenario, the LS is compatible with a significant component of strike-slip displacement and it may be subject to minor contractional motion depending on the deviation of individual fault segments from the orientation of $\sigma 1$. A strike-with minor oblique-slip on the LS faults would have created a subdued scarp along these faults, although we cannot exclude the existence of unlinked segments. Furthermore, the geometric relationship between the average trace of LS faults (Figure 4, green rose diagram) and the orientation of the maximum horizontal stress derived from the integrated VS and CS data lead us to infer the occurrence of dextral strike-slip and minor, local transpression on the LS. Similarly, the CS faults, based on their trend, would be characterized by a left-transpressional motion, and this inference is confirmed by the 60° rake derived from CR/Duccio-α.

The finding that oblique motion acted at regional scale on some fault systems of Mercury supports and complements the results of Galluzzi et al. (2015) based on fault-slip data collected from faulted craters, of

Table 1
Fault-Slip Data From Faulted Crater Analysis

Scarp/Crater	Crater ID[a]	Lat. N	Lon. E	Diam. (km)	Horizontal offset Δx (m)	Vertical offset Δh (m)	Trend	Strike	Fault true dip δ	Fault rake λ
VR/Enheduanna	05-C	48.4°	−33.8°	113	6,780 ± 968	1,217 ± 5	91 ± 13°	182° ± 2°	10 ± 1°	91 ± 13°
ER/unnamed	New	39.9°	−28.2°	16	1,294 ± 129	141 ± 13	91 ± 9°	173° ± 2°	6 ± 1°	82 ± 9°
AD/Geddes	04-B	27.1°	−29.6°	89	5,459 ± 951	840 ± 4	94 ± 17°	184° ± 2°	9 ± 2°	91 ± 17°
CR/Duccio α	01-A	58.1°	−52.5°	120	3,291 ± 467	1,507 ± 13	264 ± 37°	322° ± 3°	28 ± 10°	61 ± 31°
CR/Duccio β	02-A	57.5°	−52.3°	20	1,301 ± 130	1,619 ± 8	229 ± 23°	308° ± 3°	52 ± 4°	83 ± 10°
CR/Duccio γ	03-A	58.9°	−55.0°	23	1,727 ± 253	1,448 ± 7	246 ± 35°	336° ± 3°	40 ± 4°	90 ± 23°

[a]From Galluzzi et al. (2015).

Massironi, di Achille, et al. (2015), who studied lateral ramps associated with Enterprise Rupes and Beagle Rupes, and of Crane and Klimczak (2019), who interpreted the sigmoidal rises located in the northern smooth plains as restraining bends.

Regarding the VEA array and the VS in general, the ENE-WSW-oriented maximum compressional stress leads us to infer that the lozenge-shaped distribution of fault segments involves the alternation of NW-SE and NE-SW trending fault segments as main thrusts and oblique ramps (see Peacock et al., 2016), respectively. The N-S tectonic pattern of VS found in the H-2 quadrangle is in accordance with predictions of global contraction and tidal despinning processes acting together (Dombard & Hauck, 2008; Klimczak et al., 2015; Matsuyama and Nimmo, 2009). Nonetheless, we observe a striking similarity between the VS and CS patterns, and the models by Matsuyama and Nimmo (2009) that predict, in addition to N-S thrust systems, a NW-SE strike at high-latitudes and at the longitude of the H-2 quadrangle. Hence, VS and CS are reasonably the main systems that formed in response to the predicted global contraction and tidal despinning processes. However, no models predict NE-SW-oriented faults in this area (i.e., the LS faults, which have an inferred strike-slip motion), except for empirical tidal despinning models (Melosh, 1977). Thus, it is possible that the global tectonic models do not take into consideration other factors, such as the formation of thrust lateral ramps (e.g., Massironi, di Achille et al., 2015), or the existence of other systems that accommodate lateral deformation due to crustal heterogeneities. Importantly, we observe that LS faults are almost absent on the VEA bulge. Because the formation of the bulge was plausibly related to the displacement on the VEA and CR arrays, it seems that this structure functioned as a tectonic barrier for the development of the LS system. In this view, crustal heterogeneities linked to the geomechanical diversity of Mercury's crust are here invoked as responsible for controlling the distribution of faults acting in the post-3.7 Ga displacement field.

4.2. Interaction Between Fault Systems and the HMR

The HMR, located in the western part of H-2, covers almost 50% of the quadrangle (Figure 9a). It highlights a geochemical dichotomy that broadly corresponds to the spatial difference in the distribution of VS versus LS structures (Figure 4). Specifically, whereas LS faults are mostly found within the HMR, VS and CS form the eastern and the northeastern boundary of the region. The spatial correlation between the terrain geochemistry and the regional tectonic pattern reconstructed in this work leads to important insights on the evolution and orientation of faults. Namur and Charlier (2017) analyzed the mineralogical variability of Mercury's crust, concluding that a nonconstant density is observed across the planet. The HMR, in fact, is supposedly constituted mainly by a forsterite-dominated crust (Figure 9b), implying a density that approaches that of the mantle, in contrast with the surrounding lower-density plagioclase-rich terrains (Figure 9c; Namur & Charlier, 2017).

We argue that this lateral density contrast has controlled the nucleation of tectonic discontinuities along the HMR boundaries. Because of their resolution, the X-ray spectrometer data sets (Nittler et al., 2016) do not provide evidence whether the contrast between the HMR and the surrounding regions is sharp or diffuse. Nonetheless, we take a converse approach and suggest that the distribution of fault systems with consistent trends suggests that the boundary between the geochemical terranes is clear. In fact, the CS faults bound the

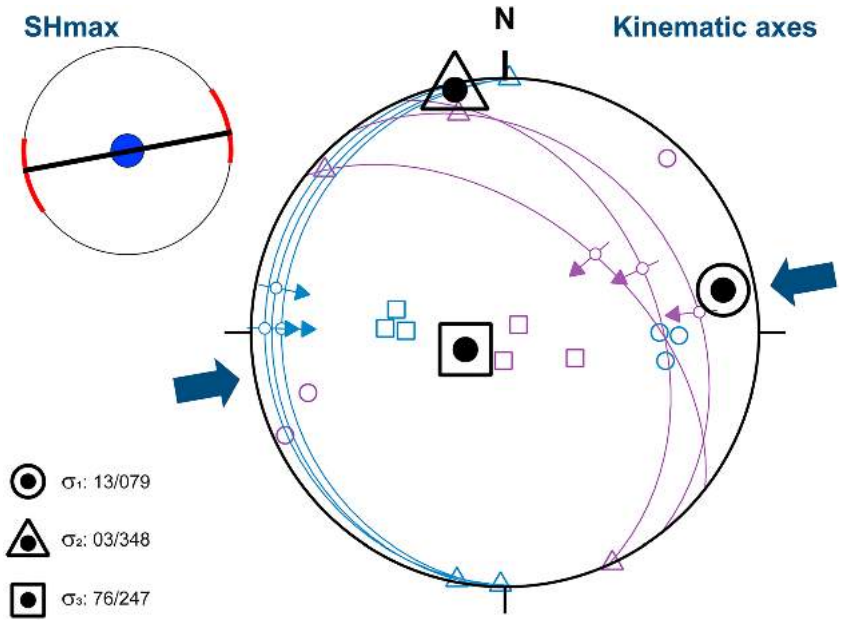

Figure 8. Stress-inversion analysis made with the PBT-axes (or pressure-tension) method (Sperner et al., 1993) derived from the data presented in Table 1. Top left: average direction of the maximum compressional strain (SHmax) with its associated standard deviation (red arcs). Right: fault planes with arrows pointing toward the motion of the hanging wall block (blue, VEA; purple, CR), with their associated P-axis (pressure, empty dots), B-axis (neutral, empty triangles), and T-axis (tension, empty squares). The principal stress axes are represented by the black symbols also reported in the legend. Numbers associated with the principal stress axes are the plunge/trend values. The blue arrows represent the maximum compressional stress direction.

HMR to the north, following its northeastern boundary (Figure 9a). The VEA array is located to the east of the HMR and apparently follows a belt of lower-density material enhanced by the plagioclase distribution map by Namur & Charlier, 2017; Figure 9c). The high-forsterite abundance seems to continue to the southwest aligned with Sector LS/*3b* (arrows in Figure 9b). Conversely, the VS segments pertaining to VEA/*ER*, VEA/*AD*, VS-2, and VS-3 run within a high-plagioclase area (higher than the NVP, Figure 9c). Despite the paucity of compositional data in this region, this high-plagioclase area broadly corresponds to the eastern ImP patch in the geological map of Galluzzi et al., 2016; cf. Figure 3). Although LS faults are largely developed within the HMR, and not at its boundaries, we believe that their origin is connected to the presence of this geochemical terrane. In particular, Sector LS/*3b* is aligned with a marked indentation of the HMR (arrow in Figure 9a). A similar alignment is observed in the forsterite distribution map by Namur and Charlier (2017), especially for Array LS-1 and Sector LS/*3b* (Figure 9b), if we exclude the presence of artifacts. Summarizing, we observe that the N-S system largely developed on the lower-density crust, while the NE-SW system sparsely broke through a higher-density region, at the margin of indenting shapes.

A spatial correspondence between structure distribution and compositional terranes is similarly evident when structures are compared with crustal thickness changes (Mazarico et al., 2014; Figure 9d). In detail, the LS-3 array that runs within the HMR bounds to the south the area of lowest-crustal thickness, which in Figure 9a is expressed by the northeastern indentation of the HMR. The CS-1 array and CR form the northeastern border of this low-thickness area (Figure 9d). The structural pattern of the quadrangle is thus tuned with the chemical and physical characteristics of the crust. This correspondence leads us to argue that the structural pattern formed so as to follow the existing compositional variations, and the high-density HMR played a major role in controlling the structural fabrics of this area of Mercury.

4.3. Tectonic Evolution of the H-2 Quadrangle

Further hints on the tectonic evolution of the H-2 quadrangle are gathered by comparing the observed structural–compositional relationships to the morpho-stratigraphy of this area. Following Galluzzi et al. (2016),

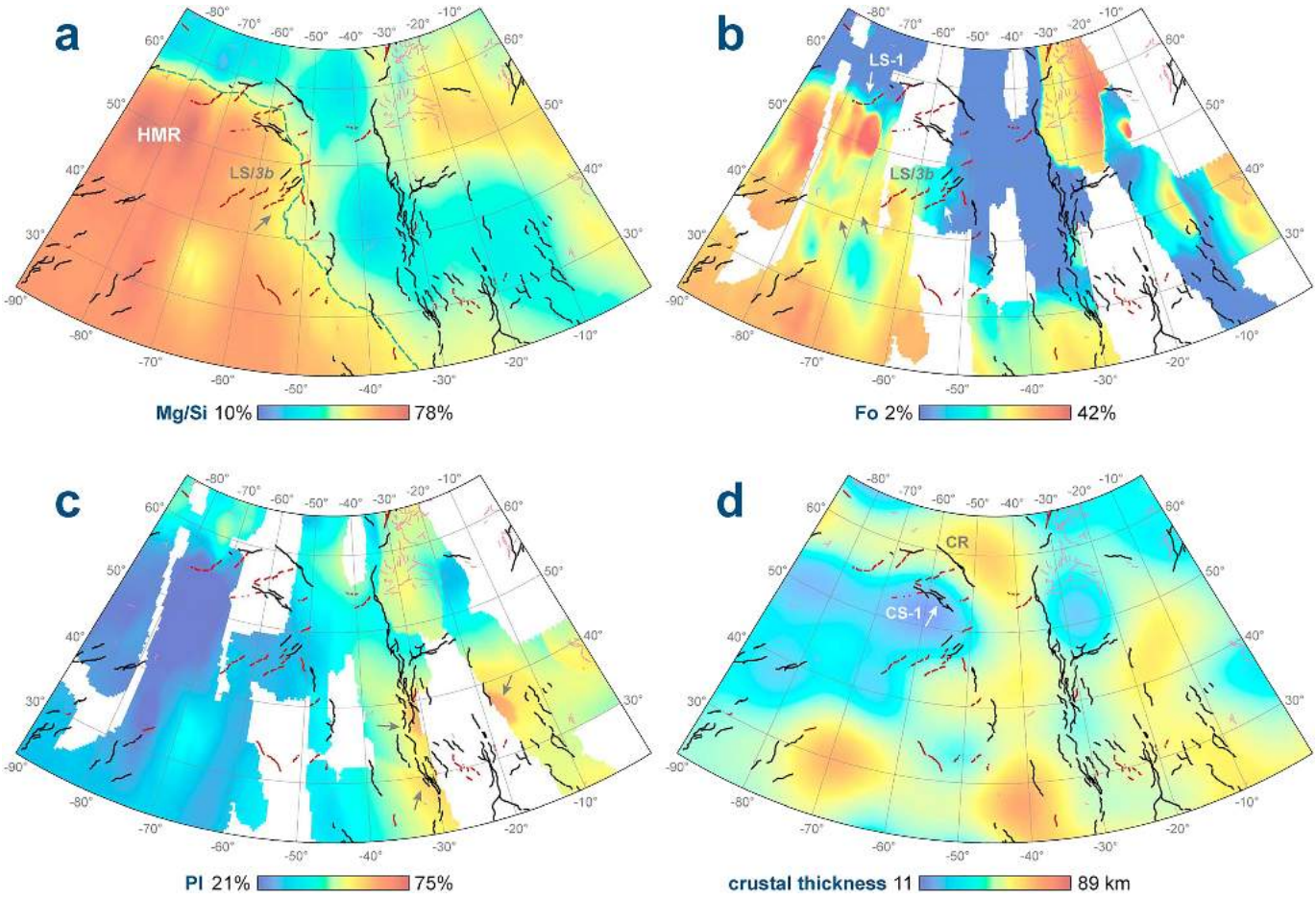

Figure 9. Faults of the H-2 quadrangle (legend in Figure 3) superimposed onto (a) the X-ray spectrometer Mg/Si abundance calculated by Nittler et al. (2016), where a green-dashed smoothed contour enhances the outer HMR boundary (~50% Mg/Si), and the gray arrow indicates an indentation in the HMR aligned with Sector LS/*3b*; (b) the forsterite (Fo) abundances estimated by Namur and Charlier (2017), where the gray arrows indicate a Fo high abundance elongated in the direction of Sector LS/*3b*, and the white arrows indicate other observed alignments; (c) plagioclase (Pl) abundances estimated by Namur and Charlier (2017), where the gray arrows indicate the highest abundances in the map; and (d) the crustal thickness derived from the HgM005 solution by Mazarico et al. (2014).

the three main mapped units are thought to reflect as many distinct events in the geological evolution of the planet, based on crater stratigraphic relationships and crater counting analysis. In the following, we use the established stratigraphy and the structural and compositional observations presented in the previous paragraphs to reconstruct critical time steps in the tectonic evolution of the quadrangle (Figure 10).

4.3.1. Early Stage: Tidal Despinning and Global Contraction

When tidal despinning and global contraction overlapped, before the early Calorian, a preferential N-S structural pattern formed at these latitudes (e.g., Klimczak et al., 2015; Matsuyama and Nimmo, 2009). It is possible that these preferential patterns were initially represented by joints (Klimczak et al., 2015), or by subparallel folds that accommodated the contractional strain before (and even after) faults broke through the crust (e.g., Byrne et al., 2014; Dombard & Hauck, 2008; Hauck et al., 2004). We stress that N-S patterns are predicted at all longitudes by some tectonic models (Dombard & Hauck, 2008; Klimczak et al., 2015; Matsuyama and Nimmo, 2009), however, a prominent N-S alignment as long as the VEA array can be observed only in this area of Mercury. Although it is not ascertained when the HMR (thought to be related to lateral heterogeneities in a poorly mixed mantle, Frank et al., 2017) actually formed, its presence during this stage cannot be ruled out (Figure 10a).

4.3.2. Intermediate Stage: Global Contraction and HMR Impact on the Strain Field

Global contraction continued during the early Calorian period, with the main faults breaking through the surface. Albeit this tectonic process should cause isotropic stresses (Klimczak et al., 2015; Massironi, di

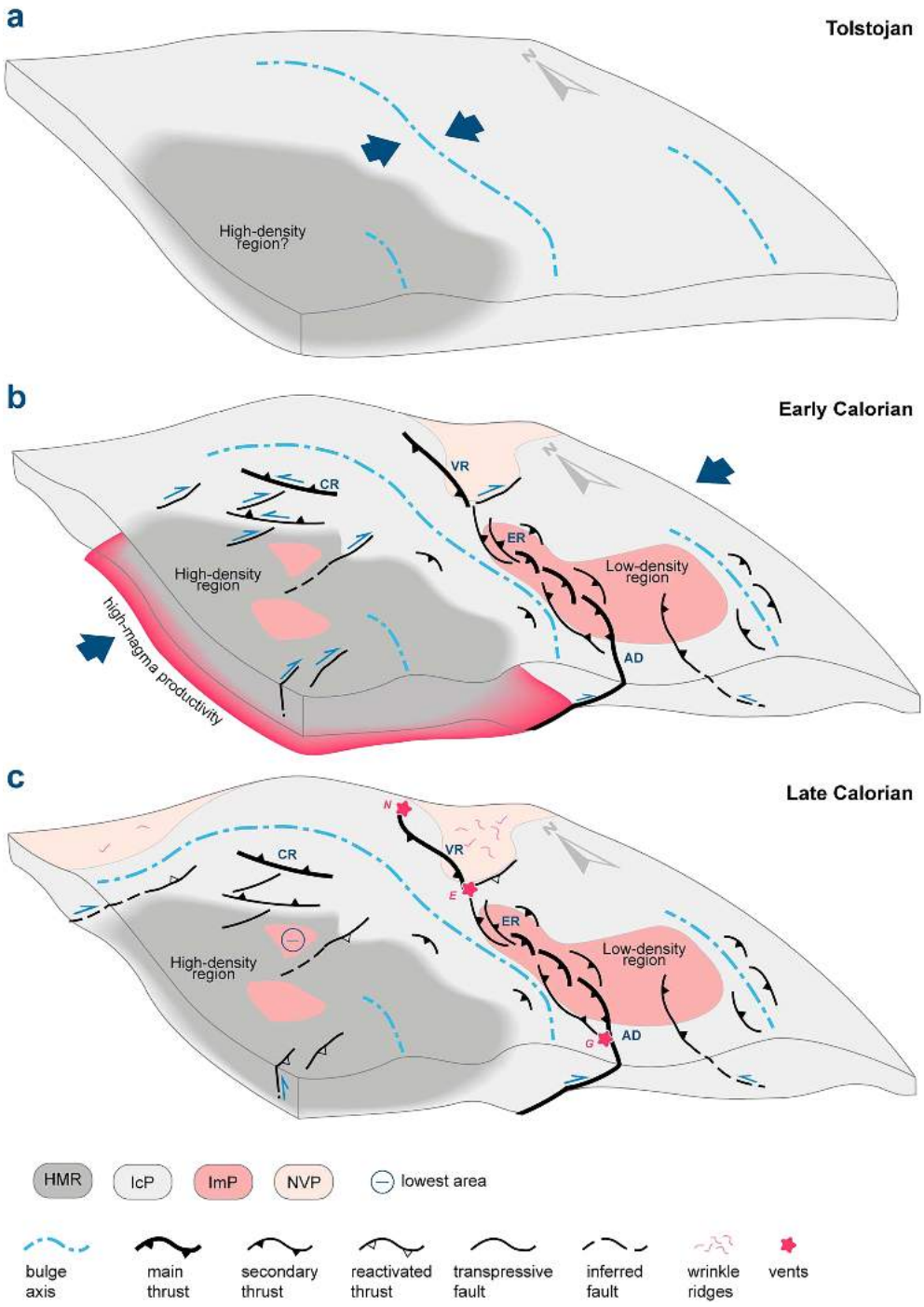

Figure 10. Block diagrams showing the hypothesized evolution of the H-2 quadrangle fault systems (not to scale). (a) Early stage, when bulges form to accommodate the shortening strain with the hypothesized preferential orientations; (b) intermediate stage, when thrust and transpressional faults develop in response to stress focused by the discontinuities of the high-Mg region (here considered as a high-density region), which is also causing resurfacing processes (ImP patches); (c) late stage, when some transpressional faults are reactivated as thrusts, the NVP embay the existing topographic relief, and vents form as a final degassing stage. The red letters indicate Namatjira (N), Enheduanna (E), and Geddes (G) vent-bearing craters.

Achille, et al., 2015), our analysis records a stress field with an ENE-WSW trending horizontal compressional axis that acted up to 3.7 Ga. We suggest that the HMR worked as a dense block, whose north and east borders concentrated and guided the global contraction stresses (Figure 10b). This eventually led to the nucleation of thrusts along the boundaries of the inherited N-S bulge, giving rise

to the prominent VEA fold-and-thrust belt. The LS and CS, which formed consistently within the same stress field, may have accommodated the lateral deformation due to the existing geochemical discontinuities and, in turn, may have deformed the HMR itself. At the beginning of this stage, it is possible that resurfacing events happened, due to the high-rate magma productivity of the HMR (Namur & Charlier, 2017) bringing to the formation of ImP within and at the borders of the HMR, as well as to the east of the VEA bulge (Figure 3; see also the units' relative ages in Galluzzi et al., 2016). The western part of the ImP patch located in correspondence of the VEA/*ER* sector has an elongated shape (Figure 3) possibly caused by the pervasive NNW-SSE thrusts within that sector. In fact, Crane and Klimczak (2017) stress how most thrusts associated to lobate scarps could have formed in a time period on the order of hundreds of Ma and much of the shortening was accommodated in the Calorian. Therefore, the formation of the numerous NNW-SSE thrust segments, which cut the ImP unit (Figure 3), may have formed just by the end of the early Calorian.

4.3.3. Late Stage: Global Contraction and Pyroclastic Activity

The NVP embayed all the tectonic rises formed in the previous stages, most probably starting from the VEA bulge, based on the observation that that area of NVP looks morphologically older (Figure S5) and is cut by VR (Figure 3). In this final stage, the stress field with ENE-WSW shortening axis ended at or soon after the early Calorian. Since during this period global contraction was the sole active tectonic process, wrinkle ridges formed with mostly random orientations, but they also partially exploited preferential ~E-W orientation of basement faults (Crane and Klimczak, 2019), or NNW-SSE orientations from the nearby VS system (pink rose diagram, Figure 4). Based on the observation that a few of the NE-SW segments are associated with scarps (Figure 3), it is possible that, during this stage, these early strike-slip faults were locally affected by a limited late reactivation as thrust faults (not enough to be recorded by the cratering retention age; Figure 10c). This is because of the continuous isotropic contraction, which is thought to be long-lived because of the young age of some fault segments (Banks et al., 2015; Watters et al., 2016). However, we cannot exclude that their relief could be due also to the before mentioned localized transpressional effects on the LS during the previous stage. Thomas et al. (2014b) dated pyroclastic deposits associated with volcanic vents across the planet finding a range of activity between 3.9 and 1.7 Ga. Based on these observations, and on the fact that the observed faults cut the vent-bearing craters and not the vents, the pyroclastic activity along the VEA array overprints the motion of the major faults in this area and is thus younger than 3.7 Ga. On Mercury, the occurrence of volcanic vents is often linked to the presence of faults (e.g., Rothery et al., 2014; Thomas et al., 2014a), and this is also observed on Earth, where relevant upwelling of hot material (forming volcanoes, geothermal manifestations, and vents) typically happens in correspondence to fault intersections (e.g., Acocella & Funiciello, 2006). A statistical analysis of vent distribution on Mercury reveals that since fault and impact crater damage zones are pervasive on the planet, there is no strict correlation between vents and faults at a global scale (Klimczak et al., 2018). However, the vents that we consider in this regional structural context are unequivocally located in correspondence to boundaries of the VEA array sectors, confirming a tight relationship between volcanic activity and major fault segmentation along this array (Figure 10c).

4.4. Further Considerations on the VEA Low-Angle Thrusts

The fault dip angles computed for the VEA array are lower than those hypothesized in literature (between 25° and 35°, e.g., Watters & Nimmo, 2010). The lower-dip angles may be due to the presence of regolith and of a relatively thick fractured layer (up to 4.5 km, Schultz et al., 1993) that would cause a flattening of the fault planes within the mechanically weaker near-surface crust. However, also in this case, the nucleation of thrusts with angles lower than 20° is unlikely. Moreover, even if we were detecting just the fault dip near the surface where the thrusts usually shallow, this should have been observable for all analyzed faulted craters. On the contrary, we observe a wide range of dip angles associated with all kinds of craters (Table 1) consistently with what observed also in Galluzzi et al. (2015), who analyzed a higher number of faulted craters, some of which could help reconstructing the entire fault geometry where more than one crater was present along the same fault trace (e.g., see fault lateral ramps in Massironi, di Achille, et al., 2015). Moreover, the VEA thrust salients (i.e., arcs) are more pronounced and curved with respect to other steeper faults (e.g., CR) that are more linear in map view, such evidence also hints to the presence of lower-dip angles (Galluzzi et al., 2015). Hence, the occurrence of low-angle thrusts has to be analyzed carefully, by accounting also for the possible underestimation of δ as described in section 3 (i.e., we consider a maximum δ of 20°). Thrust dip angles lower than 20° may hint at a nonperfectly brittle crust where ductile shear and crystal

plasticity might have played a role (see also Rothery & Massironi, 2010) and/or at the presence of fluid or gas overpressure that, as observed on Earth, leads to the nucleation of low-angle thrusts (Hubbert & Rubey, 1959; Jaeger et al., 2007; Sibson, 2017). Indeed, the high-rate magma productivity inferred for the HMR (Namur & Charlier, 2017) may have prompted interstitial gas overpressure nourished by the volcanic degassing process. Moreover, on Earth, there are documented examples of magma ascent along reverse (Tibaldi et al., 2010) or transpressional faults (De Saint Blanquat et al., 1998; Rosenmber, 2004), when overpressure is involved. The intrusion of hot magma in shear zones should also cause nucleation of low-angle thrust faults, because of the derived strength drop within the fault rocks (Rosenberg & Handy, 2005). Hence, the observed low-angle thrusts could be further evidence of the HMR subsurface activity during the abovementioned intermediate stage (Figure 9b).

5. Summary and Conclusions

We updated the structural mapping and exploited the stratigraphic information from the geological map of the H-2 quadrangle (Galluzzi et al., 2016) and compared it to the existing petrological and geophysical data sets (Mazarico et al., 2014; Namur & Charlier, 2017; Nittler et al., 2016) in order to test proposed tectonic models for Mercury (e.g., Melosh & Dzurisin, 1978; Pechmann & Melosh, 1979; Melosh & McKinnon, 1988; Klimczak et al., 2015; Matsuyama and Nimmo, 2009). This was done by means of a local- to regional-scale structural analysis with a bottom-up approach that served to reconstruct the tectonic evolution of this area of Mercury.

The H-2 quadrangle of Mercury encompasses a well-distributed pattern of faults with NNW-SSE (VS), NE-SW (LS), and NW-SE (CS) orientations. BCC results and cross-cutting relationships reveal that all fault systems are coeval and have ages not younger than 3.7 Ga. The stress-inversion analysis performed with fault-slip data gathered by means of faulted craters analysis reveals a shortening stress field with an ENE-WSW trending shortening axis at ~3.7 Ga. Within this stress field, the VS faults moved as pure thrusts, LS faults as dextral strike-slip, and CS as sinistral transpressive faults. Moreover, we observe an existing structural dichotomy due to the spatial distribution of LS + CS segments and VS segments, which corresponds to the presence of the HMR in the western part of H-2 and of lower-density terrains in the eastern part of H-2, respectively. While VS and CS concentrate at the boundary of the HMR, LS is pervasive within its extent. Therefore, the tight relationship between fault systems distribution and the lateral crustal heterogeneities leads us to infer that the HMR played a major role in controlling the orientation and kinematics of faults in this area of Mercury. In addition, the high-rate magma production inferred for this geochemical region (Namur & Charlier, 2017) may have controlled the nucleation of low-angle thrusts due to interstitial gas and fluids overpressure, or because of the strength drop caused by sin-kinematic magma intrusion. High-fluid release occurred during the HMR activity causing the resurfacing of preexisting terrains. Finally, by the end of the contraction, volcanic venting occurred along the VEA array in correspondence to fault intersections and fault sector nodes.

Results of this work highlight the importance of incorporating the lateral mechanical heterogeneities due to geochemical variations across Mercury's crust within the tectonic models. The observation that a nonisotropic stress field with ENE principal shortening axis was active up to around 3.7 Ga in the H-2 region, at a time when global contraction is thought to be the only process at work on Mercury (e.g., Klimczak et al., 2015), suggests that a strong control was exerted by inherited lateral changes in crustal density. The overarching implication is that, within specific regions of the planet, important changes in crustal properties, existing heterogeneities, and crustal weakening due to magma intrusion can control the expression of the strain field, as well as fault geometry and evolution more than the global tectonic processes (i.e., tidal despinning coupled with global contraction). Further local- and regional-scale studies are needed to understand whether the HMR influenced fault kinematics elsewhere on the planet.

Acknowledgments
We thank O. Namur, B. Charlier, E. Mazarico, and A. Genova for providing us with the data sets presented in Figure 9. We are grateful to K. Crane and D.A. Rothery for their insightful reviews that improved this paper. We gratefully acknowledge funding from the Italian Space Agency (ASI) under ASI-INAF agreement 2017-47-H.0. We also acknowledge the use of public data from the MESSENGER archive by NASA/Johns Hopkins University Applied Physics Laboratory/Carnegie Institution of Washington. This work was built on the research carried by the first author in her PhD Thesis at DiSTAR, University of Naples "Federico II". The maps, GIS shapefiles, and buffered crater counting data that support the findings of this paper are openly available in the National Institute of Astrophysics (INAF) repository at https://doi.org/10.20371/inaf/ds/2019_00001.

References

Acocella, V., & Funiciello, R. (2006). Transverse systems along the extensional Tyrrhenian margin of central Italy and their influence on volcanism. *Tectonics*, *25*, TC2003. https://doi.org/10.1029/2005TC001845

Angelier, J. (1979). Determination of the mean principal directions of stresses for a given fault population. *Tectonophysics*, **56**(3–4), T17–T26. https://doi.org/10.1016/0040-1951(79)90081-7

Banks, M. E., Xiao, Z., Watters, T. R., Strom, R. G., Braden, S. E., Chapman, C. R., et al. (2015). Duration of activity on lobate-scarp thrust faults on Mercury. *Journal of Geophysical Research: Planets*, *120*, 1751–1762. https://doi.org/10.1002/2015JE004828

Becker, K. J., Robinson, M. S., Becker, T. L., Weller, L. A., Edmunson, K. L., Neumann, G. A., et al. (2016). First global digital elevation model of Mercury. *Lunar and Planetary Science Conference*, *47*(1903), 2959.
Beuthe, M. (2010). East–west faults due to planetary contraction. *Icarus*, *209*(2), 795–817. https://doi.org/10.1016/j.icarus.2010.04.019
Bottke, W. F. Jr., Love, S. G., Tytell, D., & Glotch, T. (2000). Interpreting the elliptical crater populations on Mars, Venus, and the Moon. *Icarus*, *145*(1), 108–121. https://doi.org/10.1006/icar.1999.6323
Bottke, W. F., Vokrouhlický, D., Minton, D., Nesvorný, D., Morbidelli, A., Brasser, R., et al. (2012). An Archaean heavy bombardment from a destabilized extension of the asteroid belt. *Nature*, *485*(7396), 78–81. https://doi.org/10.1038/nature10967
Bouley, S., Craddock, R. A., Mangold, N., & Ansan, V. (2010). Characterization of fluvial activity in Parana Valles using different age-dating techniques. *Icarus*, *207*(2), 686–698. https://doi.org/10.1016/j.icarus.2009.12.030
Byrne, P. K., Klimczak, C., Celâl Sengör, A. M., Solomon, S. C., Watters, T. R., & Hauck, S. A. II (2014). Mercury's global contraction much greater than earlier estimates. *Nature Geoscience*, *7*(4), 301–307. https://doi.org/10.1038/NGEO2097
Byrne, P. K., Ostrach, L. R., Fassett, C. I., Chapman, C. R., Denevi, B. W., Evans, A. J., et al. (2016). Widespread effusive volcanism on Mercury likely ended by about 3.5 Ga. *Geophysical Research Letters*, *43*, 7408–7416. https://doi.org/10.1002/2016GL069412
Crane, K. T., & Klimczak, C. (2017). Timing and rate of global contraction on Mercury. *Geophysical Research Letters*, *44*, 3082–3089. https://doi.org/10.1002/2017GL072711
Crane, K. T., & Klimczak, C. (2019). Tectonic patterns of shortening landforms in Mercury's northern smooth plains. *Icarus*, *317*, 66–80. https://doi.org/10.1016/j.icarus.2018.05.034
De Saint Blanquat, M., Tikoff, B., Teyssier, C., & Vigneresse, J. L. (1998). Transpressional kinematics and magmatic arcs. *Geological Society of London, Special Publication*, *135*(1), 327–340. https://doi.org/10.1144/GSL.SP.1998.135.01.21
Delvaux, D., & Sperner, B. (2003). Stress tensor inversion from fault kinematic indicators and focal mechanism data: The TENSOR program. *Geological Society of London, Special Publication*, *212*(1), 75–100. https://doi.org/10.1144/GSL.SP.2003.212.01.06
Denevi, B. W., Chabot, N. L., Murchie, S. L., Becker, K. J., Blewett, D. T., Domingue, D. L., et al. (2018). Calibration, projection, and final image products of MESSENGER's Mercury Dual Imaging System. *Space Science Reviews*, *214*(1). https://doi.org/10.1007/s11214-017-0440-y
Dombard, A. J., & Hauck, S. A. II (2008). Despinning plus global contraction and the orientation of lobate scarps on Mercury: Predictions for MESSENGER. *Icarus*, *198*(1), 274–276. https://doi.org/10.1016/j.icarus.2008.06.008
Dzurisin, D. (1978). The tectonic and volcanic history of Mercury as inferred from studies of scarps, ridges, troughs, and other lineaments. *Journal of Geophysical Research*, *83*(B10), 4883–4906. https://doi.org/10.1029/JB083iB10p04883
Fassett, C. I., & Head, J. W. III (2008). Valley network-fed, open-basin lakes on Mars: Distribution and implications for Noachian surface and subsurface hydrology. *Icarus*, *198*(1), 37–56. https://doi.org/10.1016/j.icarus.2008.06.016
Fegan, E., Rothery, D. A., Marchi, S., Massironi, M., Conway, S. J., & Anand, M. (2017). Late movement of basin-edge lobate scarps on Mercury. *Icarus*, *288*, 226–234. https://doi.org/10.1016/j.icarus.2017.01.005
Frank, E. A., Potter, R. W. K., Abramov, O., James, P. B., Klima, R. L., Mojzsis, S. J., & Nittler, L. R. (2017). Evaluating an impact origin for Mercury's high-magnesium region. *Journal of Geophysical Research: Planets*, *122*, 614–632. https://doi.org/doi.org/10.1002/2016JE005244
Galluzzi, V. (2019). Multi-mapper projects: Collaborative Mercury mapping). In H. Hargitai (Ed.), *Planetary Cartography and GIS*, Lecture Notes in Geoinformation and Cartography (pp. 207–218). Cham: Springer. https://doi.org/10.1007/978-3-319-62849-3_9
Galluzzi, V., di Achille, G., Ferranti, L., Popa, C., & Palumbo, P. (2015). Faulted craters as indicators for thrust motions on Mercury. *Geological Society of London, Special Publication*, *401*(1), 313–325. https://doi.org/10.1144/SP401.17
Galluzzi, V., Guzzetta, L., Ferranti, L., di Achille, G., Rothery, D. A., & Palumbo, P. (2016). Geology of the Victoria quadrangle (H02), Mercury. *Journal of Maps*, *12*(sup1), 227–238. https://doi.org/10.1080/17445647.2016.1193777
Gault, D. E., & Wedekind, J. A. (1978). Experimental studies of oblique impact. Paper presented at the 9th Lunar and Planetary Science Conference, 3843–3875.
Giacomini, L., Massironi, M., Galluzzi, V., Ferrari, S., & Palumbo, P. (2018). How old are Mercury's thrust systems? New results and implications for the thermal evolution of the planet. In Mercury: Current and Future Science of the Innermost Planet, LPI Contribution No. 2047, 2018, id.6076.
Giacomini, L., Massironi, M., Marchi, S., Fassett, C. I., di Achille, G., & Cremonese, G. (2015). Age dating of an extensive thrust system on Mercury: Implications for the planet's thermal evolution. *Geological Society of London, Special Publication*, *401*(1), 291–311. https://doi.org/10.1144/SP401.21
Gilbert, G. K. (1893). *The Moon's face: A study of the origin of its features*. Washington: Philosophical Society of Washington.
Grott, M., Breuer, D., & Laneuville, M. (2011). Thermo-chemical evolution and global contraction of Mercury. *Earth and Planetary Science Letters*, *307*(1-2), 135–146. https://doi.org/10.1016/j.epsl.2011.04.040
Hauck, S. A. II, Dombard, A. J., Phillips, R. J., & Solomon, S. C. (2004). Internal and tectonic evolution of Mercury. *Earth and Planetary Science Letters*, *222*(3-4), 713–728. https://doi.org/10.1016/j.epsl.2004.03.037
Hawkins, S. E., Boldt, J. D., Darlington, E. H., Espiritu, R., Gold, R. E., Gotwols, B., et al. (2007). The Mercury dual imaging system on the MESSENGER spacecraft. *Space Science Reviews*, *131*(1-4), 247–338. https://doi.org/10.1007/s11214-007-9266-3
Hoke, M. R., & Hynek, B. M. (2009). Roaming zones of precipitation on ancient Mars as recorded in valley networks. *Journal of Geophysical Research*, *114*, E08002. https://doi.org/10.1029/2008JE003247
Hubbert, M. K., & Rubey, W. W. (1959). Mechanics of fluid-filled porous solids and its application to overthrust faulting. *Bulletin of the Geological Society of America*, *70*(2), 115–166. https://doi.org/10.1130/0016-7606(1959)70[115:ROFPIM]2.0.CO;2
Jaeger, J. C., Cook, N. G. W., & Zimmerman, R. W. (Eds) (2007). *Fundamentals of rock mechanics*, (4th ed.). Oxford: Blackwell Publishing.
Jenness, J. (2011). Tools for graphics and shapes: Extension for ArcGIS. Jenness Enterprises. Available at: http://www.jennessent.com/arcgis/shapes_graphics.htm
Jenness, J. (2014). Polar plots for ArcGIS. Jenness Enterprises. Available at: http://www.jennessent.com/arcgis/polar_plots.htm
Kenkmann, T., Poelchau, M. H., & Wulf, G. (2014). Structural geology of impact craters. *Journal of Structural Geology*, *62*, 156–182. https://doi.org/10.1016/j.jsg.2014.01.015
Kerber, L., Head, J. W., Solomon, S. C., Murchie, S. L., Blewett, D. T., & Wilson, L. (2009). Explosive volcanic eruptions on Mercury: Eruption conditions, magma volatile content, and implications for interior volatile abundances. *Earth and Planetary Science Letters*, *285*(3-4), 263–271. https://doi.org/10.1016/j.epsl.2009.04.037
King, S. D. (2008). Pattern of lobate scarps on Mercury's surface reproduced by a model of mantle convection. *Nature Geoscience*, *1*(4), 229–232. https://doi.org/10.1038/ngeo152
Klimczak, C., Byrne, P. K., & Solomon, S. C. (2015). A rock-mechanical assessment of Mercury's global tectonic fabric. *Earth and Planetary Science Letters*, *416*, 82–90. https://doi.org/10.1016/j.epsl.2015.02.003

Klimczak, C., Crane, K. T., Habermann, M. A., & Byrne, P. K. (2018). The spatial distribution of Mercury's pyroclastic activity and the relation to lithospheric weaknesses. *Icarus*, *315*, 115–123. https://doi.org/10.1016/j.icarus.2018.06.020

Kneissl, T., Michael, G. G., Platz, T., & Walter, S. H. G. (2015). Age determination of linear surface features using the Buffered Crater Counting approach–Case studies of the Sirenum and Fortuna Fossae graben systems on Mars. *Icarus*, *250*, 384–394. https://doi.org/10.1016/j.icarus.2014.12.008

Kneissl, T., van Gasselt, S., & Neukum, G. (2011). Map-projection-independent crater size-frequency determination in GIS environments—New software tool for ArcGIS. *Planetary and Space Science*, *59*(11-12), 1243–1254. https://doi.org/10.1016/j.pss.2010.03.015

Korteniemi, J., Walsh, L. S., & Hughes, S. S. (2015). Wrinkle ridge. In H. Hargitai, & Á. Kereszturi (Eds.), *Encyclopedia of Planetary Landforms* (pp. 2324–2331). New York: Springer Science+Business Media. https://doi.org/10.1007/978-1-4614-3134-3

Le Feuvre, M., & Wieczorek, M. A. (2011). Nonuniform cratering of the Moon and a revised crater chronology of the inner Solar System. *Icarus*, *214*(1), 1–20. https://doi.org/10.1016/j.icarus.2011.03.010

Marchi, S., Chapman, C. R., Fasset, C. I., Head, J. W., Bottke, W. F., & Strom, R. G. (2013). Global resurfacing of Mercury 4.0–4.1 billion years ago by heavy bombardment and volcanism. *Nature*, *499*(7456), 59–61. https://doi.org/10.1038/nature12280

Massironi, M., & Byrne, P. K. (2015). High-relief ridge. In H. Hargitai, & Á. Kereszturi (Eds.), *Encyclopedia of Planetary Landforms* (pp. 932–934). New York: Springer Science+Business Media. https://doi.org/10.1007/978-1-4614-3134-3

Massironi, M., Byrne, P. K., & van der Bogert, C. H. (2015). Lobate scarp. In H. Hargitai, & Á. Kereszturi (Eds.), *Encyclopedia of Planetary Landforms* (pp. 1255–1262). New York: Springer Science+Business Media. https://doi.org/10.1007/978-1-4614-3134-3

Massironi, M., di Achille, G., Rothery, D. A., Galluzzi, V., Giacomini, L., Ferrari, S., et al. (2015). Lateral ramps and strike-slip kinematics on Mercury. *Geological Society of London, Special Publication*, *401*(1), 269–290. https://doi.org/10.1144/SP401.16

Matsuyama, I., & Nimmo, F. (2009). Gravity and tectonic patterns of Mercury: Effect of tidal deformation, spin-orbit resonance, nonzero eccentricity, despinning, and reorientation. *Journal of Geophysical Research*, *114*, E01010. https://doi.org/10.1029/2008je003252

Mazarico, E., Genova, A., Goossens, S., Lemoine, F. G., Neumann, G. A., Zuber, M. T., et al. (2014). The gravity field, orientation, and ephemeris of Mercury from MESSENGER observations after three years in orbit. *Journal of Geophysical Research: Planets*, *119*, 2417–2436. https://doi.org/10.1002/2014JE004675

Melosh, H. J. (1977). Global tectonics of a despun planet. *Icarus*, *31*(2), 221–243. https://doi.org/10.1016/0019-1035(77)90035-5

Melosh, H. J., & Dzurisin, D. (1978). Mercurian global tectonics: A consequence of tidal despinning? *Icarus*, *35*(2), 227–236. https://doi.org/10.1016/0019-1035(78)90007-6

Melosh, J. H., & McKinnon, W. B. (1988). The tectonics of Mercury. In F. Vilas, C. R. Chapman, & M. Matthews (Eds.), *Mercury* (pp. 374–400). Tucson, Arizona: University of Arizona Press.

Michael, G. G., & Neukum, G. (2010). Planetary surface dating from crater size-frequency distribution measurements: Partial resurfacing events and statistical age uncertainty. *Earth and Planetary Science Letters*, *294*(3-4), 223–229. https://doi.org/10.1016/j.epsl.2009.12.041

Michel, N. C., Hauck, S. A. II, Solomon, S. C., Phillips, R. J., Roberts, J. H., & Zuber, M. T. (2013). Thermal evolution of Mercury as constrained by MESSENGER observations. *Journal of Geophysical Research: Planets*, *118*, 1033–1044. https://doi.org/10.1002/jgre.20049

Namur, O., & Charlier, B. (2017). Silicate mineralogy at the surface of Mercury. *Nature Geoscience*, *10*(1), 9–13. https://doi.org/10.1038/ngeo2860

Nittler, L. R., Frank, E. A., Weider, S. Z., Crapster-Pregont, E., Vorburger, A., Starr, R. D., Solomon, S. C. (2016). Global major-element maps of Mercury updated from four years of MESSENGER X-ray observations. Lunar and Planetary Science Conference, 47, 1237.

Pappalardo, R. T., & Collins, G. C. (2005). Strained craters on Ganymede. *Journal of Structural Geology*, *27*(5), 827–838. https://doi.org/10.1016/j.jsg.2004.11.010

Peacock, D. C. P., Nixon, C. W., Rotevatn, A., Sanderson, D. J., & Zuluaga, L. F. (2016). Glossary of fault and other fracture networks. *Journal of Structural Geology*, *92*, 12–29. https://doi.org/10.1016/j.jsg.2016.09.008

Pechmann, J. B., & Melosh, H. J. (1979). Global fracture patterns of a despin planet application to Mercury. *Icarus*, *38*(2), 243–250. https://doi.org/10.1016/0019-1035(79)90181-7

Redmond, H. L., & King, S. D. (2007). Does mantle convection currently exist on Mercury? *Physics of the Earth and Planetary Interiors*, *164*(3-4), 221–231. https://doi.org/10.1016/j.pepi.2007.07.004

Rosenberg, C. L., & Handy, M. R. (2005). Experimental deformation of partially melted granite revisited: Implications for the continental crust. *Journal of Metamorphic Geolology*, *23*(1), 19–28. https://doi.org/10.1111/j.1525-1314.2005.00555.x

Rosenmber, C. L. (2004). Shear zones and magma ascent: A model based on a review of the Tertiary magmatism in the Alps. *Tectonics*, *23*, TC3002. https://doi.org/10.1029/2003TC001526

Rothery, D. A., & Massironi, M. (2010). Beagle Rupes–evidence for a basal decollement of regional extent in Mercury's lithosphere. *Icarus*, *209*(1), 256–261. https://doi.org/10.1016/j.icarus.2009.12.009

Rothery, D. A., Thomas, R. J., & Kerber, L. (2014). Prolonged eruptive history of a compound volcano on Mercury: Volcanic and tectonic implications. *Earth and Planetary Science Letters*, *385*, 59–67. https://doi.org/10.1016/j.epsl.2013.10.023

Schultz, R. A. (1993). Brittle strength of basaltic rock masses with applications to Venus. *Journal of Geophysical Research*, *98*(E6), 10,883–10,895. https://doi.org/10.1029/93JE00691

Schultz, R. A. (2000). Localization of bedding plane slip and backthrust faults above blind thrust faults: Keys to wrinkle ridge structure. *Journal of Geophysical Research*, *105*(E5), 12,035–12,052. https://doi.org/10.1029/1999JE001212

Shoemaker, E. M. (1962). Interpretation of lunar craters. In Z. Kopal (Ed.), *Physics and astronomy of the moon* (pp. 283–359). New York–London: Academic Press.

Sibson, R. H. (2017). Tensile overpressure compartments on low-angle thrust faults. *Earth, Planets and Space*, *69*(1), 113. https://doi.org/10.1186/s40623-017-0699-y

Solomon, S. C., McNutt, R. L. Jr., Gold, R. E., & Domingue, D. L. (2007). MESSENGER mission overview. *Space Science Reviews*, *131*(1-4), 3–39. https://doi.org/10.1007/s11214-007-9247-6

Sperner, B., Ratschbacher, L., & Ott, R. (1993). Fault-striae analysis: A Turbo-Pascal program package for graphical presentation and reduced stress tensor calculation. *Computers and Geosciences*, *19*(9), 1361–1388. https://doi.org/10.1016/0098-3004(93)90035-4

Strom, R. G., Trask, N. J., & Guest, J. E. (1975). Tectonism and volcanism on Mercury. *Journal of Geophysical Research*, *80*(17), 2478–2507. https://doi.org/10.1029/JB080i017p02478

Tanaka, K. L. (1982). A new time-saving crater-count technique with application to narrow features. NASA Technical Memorandum, TM-85127, 123–125

Thomas, R. J., Rothery, D. A., Conway, S. J., & Anand, M. (2014a). Mechanisms of explosive volcanism on Mercury: Implications from its global distribution and morphology. *Earth and Planetary Science Letters*, *431*, 164–172. https://doi.org/10.1016/j.epsl.2015.09.029

Thomas, R. J., Rothery, D. A., Conway, S. J., & Anand, M. (2014b). Long-lived explosive volcanism on Mercury. *Geophysical Research Letters*, *431*, 164–172. https://doi.org/10.1016/j.epsl.2015.09.029

Tibaldi, A., Pasquarè, F. A., & Tormey, D. (2010). Volcanism in reverse and strike-slip fault settings. In S. Cloetingh, & J. Negendank (Eds.), *New frontiers in integrated solid earth sciences* (pp. 315–348). Dordrecht: Springer-Verlag. https://doi.org/10.1007/978-90-481-2737-5

Tosi, N., Grott, M., Plesa, A.-C., & Breuer, D. (2013). Thermochemical evolution of Mercury's interior. *Journal of Geophysical Research: Planets*, *118*, 2474–2487. https://doi.org/10.1002/jgre.20168

Watters, T., Daud, K., Banks, M., Selvans, M., Chapman, C., & Ernst, C. (2016). Recent tectonic activity on Mercury revealed by small thrust fault scarps. *Nature Geoscience*, *9*(10), 743–747. https://doi.org/10.1038/ngeo2814

Watters, T. R. (1988). Wrinkle ridge assemblages on the terrestrial planets. *Journal of Geophysical Research*, *93*(B9), 10,236–10,254. https://doi.org/10.1029/JB093iB09p10236

Watters, T. R., & Nimmo, F. (2010). The tectonics of Mercury. In T. R. Watters, & R. A. Schultz (Eds.), *Planetary Tectonics* (pp. 15–80). New York: Cambridge University Press.

Watters, T. R., Robinson, M. S., Bina, C. R., & Spudis, P. D. (2004). Thrust faults and the global contraction of Mercury. *Geophysical Research Letters*, *31*, L04071. https://doi.org/10.1029/2003GL019171

Yue, Z., Michael, G. G., Di, K., & Liu, J. (2017). Global survey of lunar wrinkle ridge formation times. *Earth and Planetary Science Letters*, *477*, 14–20. https://doi.org/10.1016/j.epsl.2017.07.048

Weider, S. Z., Nittler, L. R., Starr, R. D., Crapster-Pregont, E. J., Peplowski, P. N., Denevi, B. W., et al. (2015). Evidence for geochemical terranes on Mercury: Global mapping of major elements with MESSENGER's X–Ray Spectrometer. *Earth and Planetary Science Letters*, *416*, 109–120. https://doi.org/10.1016/j.epsl.2015.01.023

Zuber, M. T., Smith, D. E., Phillips, R. J., Solomon, S. C., Neumann, G. A., Hauck, S. A., et al. (2012). Topography of the northern hemisphere of Mercury from MESSENGER laser altimetry. *Science*, *336*(6078), 217–220. https://doi.org/10.1126/science.1218805